Cancer Protrusions on a Tightrope – Suspended Fiber Platform Reveals Protrusion Dynamics Independent of Cell Migration

Brian J. Koons

Thesis submitted to the faculty of the Virginia Polytechnic Institute and State University in partial fulfillment of the requirements for the degree of

Master of Science

In

Mechanical Engineering

Amrinder S. Nain, Chair

Bahareh Behkam

Rakesh K. Kapania

April 29, 2015

Blacksburg, Virginia

Keywords: nanofiber, protrusion, curvature, cancer cell

Cancer Protrusions on a Tightrope – Suspended Fiber Platform Reveals Protrusion Dynamics Independent of Cell Migration

Brian J. Koons

ABSTRACT

Indispensable to all modes of migration used during single cell metastasis, cytoplasmic protrusions are pivotal in surveying cells' local surroundings which ultimately initiates migration of the cell body. Cancer cell migration is fairly well studied with the traditional focus on protrusion driven cell body displacement, while less is known on the role of protrusions in sensing cellular microenvironments. Here, we present a suspended and aligned fiber platform capable of high spatio-temporal imaging of protrusions capable of sensing fiber curvature contrasts independent of cell migration. By varying the diameter of suspended fibers, we are able to maintain cell migration along low curvature-large diameter (2μm) fibers, while solely allowing cells to sense, initiate, and mature protrusions on orthogonally deposited high curvature-low diameter (~100, 200 and 600 nm) fibers. Using highly aggressive breast MDA-MB-231 and brain glioblastoma DBTRG-05MG model systems, we find that MDA-MB-231 protrusion maturation dynamics are more sensitive to changes in fiber curvature and fibronectin ligand coating concentration compared to DBTRG-05MG. Furthermore, we find that vimentin intermediate filaments localize within 70% of mature protrusions, which normally form on larger diameter fibers. Additionally, protrusion lengths fluctuate continuously until the protrusion is either terminated or stabilized, and occasionally protrusions are observed to shed cytoplasmic fragments. Through manipulation of curvature contrasts, we demonstrate single protrusive hierarchical decomposition and coordination in zeroth (main), first and second order branches. The fiber curvature platform presented here

uniquely allows cancer cells to sense nanofiber curvature contrasts, thus providing new mechanistic insights in protrusion initiation, maturation, and hierarchical coordination.

ACKNOWLEDGEMENTS

I gratefully acknowledge the support provided by Institute for Critical Technology and Applied Science (ICTAS), Virginia Tech and the Department of Mechanical Engineering, Virginia Tech. This research and time was partially funded by the Bill and Andrea Waide Research Fund, Walts Fellowship, and the Hord Fellowship. Also, special thanks goes out to the members of the STEP lab, specifically Puja Sharma, as well as a summer research intern Kabir Dhada for their insight during preliminary experimentation.

TABLE OF CONTENTS

LIST OF FIGURES

1. INTRODUCTION

Cellular protrusion and migration are often linked together, where migration is described as a three step process: protrusion extension, body translocation, and tail retraction. The leading edge is a term used describe the direction of protrusion, and in most cases, the direction of migration. However, it is often hard to analyze protrusion dynamics when the interface between the protrusion and the cell body is not distinct. Also, protrusion dynamics are hard to analyze separately from migration dynamics since they are both, on average, moving in the same direction at the same average speed. Additionally, solely studying leading edge protrusions biases studies towards analyzing protrusions' migratory function, as opposed to their equally important sensing functions. Therefore, it is important to decouple the protrusion-migration relationship in order to specifically analyze protrusion dynamics and their sensory functions.

Depending on their function and the cellular environment, pseudopodial protrusions have been observed to form many different structures. On flat surfaces, broad sheet-like protrusions, called lamellipodia, form and drive migration while smaller rod-like protrusion, called filopodia, extend further in order to sense the forthcoming environment [1], [2]. When plated on flat porous membrane, protrusion called invadopodia form and are used to help cells penetrate surfaces and migrate across membranes [3]. In 3D matrices, more complex protrusions form in order to help cells travel, create pores, and deflect adjacent fibrils [4]. The previously mentioned protrusion are driven by actin polymerization, however, protrusions can also be driven by internal hydrostatic pressure, such as lobopodia and blebs [5], [6].

Protrusion are important to study due to their migratory and sensory functions, which vital in many developmental and diseased states, such as cancer. Of all the hallmarks of cancer, protrusions are most relevant to activating invasion and metastasis [7]. In addition to protrusions,

fibers and alignment are also very important in metastatic processes. For instances of brain tumors, glioblastoma cells have been seen to migrate along aligned fiber-like neurons [8]. Also, in the case of breast tumors, the surrounding collagen fibers have been seen to align radially from the tumor and this alignment is indicative of a poor prognosis [9], [10]. The previously mentioned collagen fibers are aligned due to the stromal cell presence. It has also been seen that cancer-associated fibroblasts, stromal cells, are aligned in culture, resulting in aligned underlying fibronectin fibers, while their normal counter parts are not [11]. Therefore, in order to better understand cancer, it is very important to investigate protrusions on aligned fiber substrates.

Cancer is the transformation of a healthy microenvironment into a stiffened network of fibrous proteins populated by metastasis-provoking stromal cells. The changing extracellular matrix (ECM) gives rise to metastatic triggers and phenotypes, while also enabling the establishment of attractant gradients and migration pathways [12]. The resultant physical surroundings are composed of an architecture that, depending on its arrangement, either favors or constrains tumor cell migration and advancement to distal organs and tissues. ECM anisotropy aids invasion by providing a continuous pathway for migration at high speeds without the need for proteolytic ECM degradation [13], [14], [15]. On the other hand, dense fibrous meshwork causes miniscule pore formation requiring metastatic cells to either deform their body and nucleus or generate adequate forces to widen the opening [16].

Metastatic cellular invasion starts with individual cells sensing their immediate environment using cytoplasmic protrusions, which also provides aid for force transduction and motility [17], [18]. Protrusions are projections of cytoplasm from the primary cellular embodiment that perform a specific task, or set of tasks, with distinct temporal and morphological characteristics [19]. While the importance of protrusions in metastasis is widely acknowledged,

they are almost always examined conjointly with migration, therefore, the individual organization and dynamics of cell protrusions in 1, 2, and 3D are not fully described [16], [20], [21], [22], [23], [24], [25]. To date, cancer cell protrusions have been extensively studied using flat coated substrates, Boyden chambers, and collagen gels [26], [27]. These platforms have allowed for the investigation of how substrate properties and dimensionality influence protrusive behavior and its interplay with migration [28], [29], [30]. For breast cancer cells of various metastatic capacities, it was recently demonstrated that protrusions observed in both 2D and 3D contexts can be used to accurately predict invasiveness in 3D environments while solely observing cell migration on 2D substrates was deemed to be a poor indicator of metastatic potential [31], [32], [33], [34], [35].

Current 2D and 3D *in vitro* platforms ordinarily provide a physically homogenous mechanical environment which only partially captures the heterogeneity present in an *in vivo* tumor microenvironment. The tumor microenvironment composition consists of a variety of ECM proteins which provide structural support for migration in the form of fibers and bundles that vary in size, orientation, and mechanical properties. For instance, the diameter of individual and bundled collagen fibers have been reported to be 70 nm and up to 30 μm, respectively [36]. Accumulation of such proteins in ECM networks cause tumor stiffness to increase dramatically in certain regions; as resections of breast cancer tissue have been measured to be ten times more stiff than its healthy counterpart [37]. Metastatic cells have also been observed to travel along fiber-like tissue structures such as blood vessels and myelinated axons. Collectively, these various substrates account for many types of curvatures and topographies as well as all the spatial dimensions [36]. Additionally, supporting stromal cells have been seen to lay the groundwork for invasion by depositing additional ECM fibers, approximately 100 to 500 nm in diameter, as well as by remodeling the ECM into a wide variety of possible forms: dense or sparse, aligned or

random, and stiff or compliant [12], [38], [39]. When transitioning through and between these substrate types and configurations, protrusions allow cancer cells to sense these various properties around them. Contrasts in the physical environment provide spatial and temporal cues which cause instantaneous cell-ECM interactions that can lead to metastatic processes [40]. This interaction is composed of, first, the cell forming and extending a protrusion and, second, protrusion maturation by recruiting additional adhesion and cytoskeletal proteins, therefore, initiating possible commitment towards migration. The first step in probing this phenomenon is the development of a controlled and mechanically-defined *in vitro* environment that is capable of elucidating when, how, and where single cancer cells form protrusions with the potential to initiate or redirect intrusive migratory processes.

Cells on fiber networks are provided with simultaneous 1, 2, and 3D stimuli, as cells are elongated along the fiber axis (1D), stretch between multiple fibers (2D), and finally, wrap around the suspended fibers (3D). Furthermore, cells on suspended fibers sense the structural stiffness (N/m) and curvature independently. With increasing structural stiffness, cells have reduced migration and longer focal adhesion cluster (FAC) lengths. In contrast, at similar structural stiffness cells put out longer focal adhesion cluster lengths on smaller diameters suggesting a conservation of FAC area and also exhibit higher migration speeds on larger diameter fibers [41]. Thus, we hypothesized that if a cell were to reach an intersection of two fibers that differ in curvature, migration would be restricted to the larger diameter fiber, and therefore, protrusions would serve as the only sensing mechanism directly interacting with the smaller diameter fiber. By carefully manipulating the curvature of the smaller fibers as well as the concentration of the fibronectin coating on fibers, we were able to reveal how the characteristics and behavior of protrusions differed as a result. For MDA-MB-231 and DBTRG-05MG specifically, we

characterized protrusion length, extension and retraction rate, and morphology in addition to examining the behavior of protrusion elongation, fluctuation, and maturation. We found that a longer protrusion length and a broader morphology was associated with larger diameter fibers while the extension and retraction rates did not significantly change. Immunostaining for actin, tubulin, and vimentin demonstrated vimentin co-localizing in protrusions with increasing eccentricity, a measure of protrusion width and maturity, while actin and tubulin were present in less developed protrusions. In addition, transient examinations showed that protrusion length fluctuated throughout the extension process, providing new insights on protrusion hierarchical (zeroth, first, and second order) sensing and coordination. Depending upon the migratory state of the cell (stationary vs. migratory), we observed two dominant protrusion-specific phenotypes which provide a glimpse of how cancer cells use protrusions to inspect their immediate environment. Protrusions were also observed to be used as a tool to shed cell fragments away from the migratory path of the cell. Lastly, using an inverse mathematical model, protrusion contractile forces can be calculated from measuring fiber deflections. Altogether, the development of this platform provides detailed mechanistic knowledge in cellular protrusive behavior on suspended fibers while also addressing the impact of fiber curvature and fibronectin concentration. Our observations highlight the role of the microenvironment to either favor or hinder protrusion formation, elongation, and maturation.

2. MATERIALS AND METHODS

2.1 Fiber Manufacturing.

Polystyrene nanofibers were fabricated using previously reported Spinneret-based Tunable Engineered Parameters (STEP) technique. Using user-defined inputs, the *base fiber* diameter was made to be 2 -3 µm in diameter. *Protrusive fibers* were formed with diameters of 94.2 ± 70.1 nm (small), 202.1 ± 53.0 nm (medium), and 564.8 ± 231.4 nm (large). Fibers were deposited and suspended on polystyrene frames with 4 mm by 4 mm squares cut out of 6 mm by 6 mm sheets. Fiber samples were then treated with an in-house solvent fusing method which connects crossing fibers at their intersections to create a unified fiber network. Samples were then fixed with vacuum grease to glass-bottom six-well plates (MatTek Corp). Fixed samples were then coated with varying concentrations of fibronectin (2 µg/ml, 4 µg/ml, and 16 µg/ml). Fibers were coated for 3 hours prior to seeding.

2.2 Cell Culture and Seeding.

MDA-MB-231 (mammary ductal adenocarcinoma) cells were cultured in L-15 medium with 10% FBS and 1% penicillin. DBTRG-05MG (glioblastoma multiforme) cells were cultured in RMPI-1640 medium with 10% FBS, 1% penicillin/streptomycin, 30 mg/L L-proline, 35 mg/L L-cystine, 3.57 g/L HEPES, 15 mg/L hypoxanthine, 1 mg/L adenosine triphosphate, 10 mg/L adenine, and 1 mg/L thymidine. Cultures were maintained in incubator at 5% CO_2 and 37°C. Samples were seeded with a seeding density of 300,000 cells per ml where only a fraction would attach to fibers depending on fiber diameter and fibronectin concentration. The majority of cells rested on the glass bottom below the samples for the duration of the experiment. Samples were maintained in well plates with 2 ml per well of their respective growth medium once cell-fiber attachment was observed.

2.3 Time-lapse Microscopy and Analysis.

Samples were imaged with Carl Zeiss microscope (AxioObserver Z.1 with mRm camera) equipped with incubator within the glass-bottom six well plates. The incubator was maintained at 5% CO_2 and 37°C. Time-lapse videos were taken at a magnification of 40x with a frame imaged every minute for 6 hours. Videos were analyzed by hand using measurement tools on the Carl Zeiss Axiovision software.

2.4 Immunostaining and Fluorescent Imaging.

Cells were fixed while attached to nanofiber samples using 4% paraformaldehyde. Cells were permeabilized by soaking samples in permealization solution (0.1% Triton-X-100 in PBS) for 15 minutes. Samples were then immersed in blocking buffer (5% goat blocking buffer) for 30 minutes. Primary antibodies were diluted in antibody dilution buffer (Triton-X-100 and BSA) at the following dilution ratios: vimentin mouse monoclonal antibody (1:100), α/β-Tubulin antibody (1:100), paxillin rabbit polyclonal antibody (1:250). Secondary antibodies were diluted in antibody dilution buffer and added at the following dilution ratios: Alex Fluor 405 Goat Anti-Mouse (1:100) and Alexa Fluor 488 Goat Anti-Rabbit (1:100). Rhodamine Phalloidin was also diluted in antibody dilution buffer with a dilution ratio of 1:100. All stains were imaged using immunofluorescent microscopy with Carl Zeiss microscope. All stained samples were imaged with a 63x objective lens. Intensity plots were created using ImageJ.

2.5 Statistical Analysis.

All data was analyzed for statistical significance using GraphPad software. One, two, and three stars on plots represent $p<0.05$, $p<0.01$, and $p<0.001$, respectively. All error bars show standard error.

2.6 Force Measurement.

The experimental fiber deflection profile is formed from data collected from time-lapse videos. When a protrusion deflects a fiber, 5 coordinates are measured on the same frame. Each coordinate is a measure of the position along the fiber and the deflection at that location. The first coordinate, the intersection of the protrusive fiber and the base fiber that the cell is on, serves as a reference for the other 4 coordinates. The second coordinate is measured at the nearest cell attachment, relative to the origin. The third coordinate serves as a reference and is measured anywhere along the cell attachment length. The fourth coordinate is measured at the farther cell attachment, relative to the origin. Lastly, the fifth coordinate is measured at the opposite protrusive-base fiber intersection, therefore, it denotes the length of the fiber segment. Together, these five points represent the experimental fiber deflection profile that the theoretical mathematical program uses to match. When the theoretical fiber deflection profile matches the experimental profile, the parameters of the theoretical model are used to describe the load type and magnitude.

3. RESULTS

The analysis described in sections 3.1 to 3.8 is authored by myself and my adviser, Dr. Amrinder S. Nain, and it is currently under consideration for publication.

3.1 Geometric contrast between orthogonal fiber curvatures induce protrusions independent of cell migration.

Cellular protrusions are required for sensing the peripheral environment and, in the presence of motility-inducing feedback, they serve as the organelles responsible for the first phase of migration: initiation [20]. We examined MDA-MB-231 (breast) and DBTRG-05MG (glioblastoma) metastatic cell lines which are both highly invasive and display aggressive phenotypes. *In vivo,* alignment plays an important role in aiding invasion within both of the native environments in which these cells originated. Also, tumors in these regions are linked to high mortality rates as they are prone to metastasize [36]. In order to study the causal relationships between protrusive dynamics and metastatic ability, our goal was to design and manipulate an exquisite architecture of suspended nanofiber networks that are capable of eliciting protrusions independent of the migration of the cell body. To achieve this, we used the previously described non-electrospinning Spinneret-based Tunable Engineered Parameters (STEP) technique to fabricate fused and suspended nanofiber networks in a two layer system with high control of fiber alignment, diameter, and orientation (31–34). For the first design, we constructed an evenly spaced grid of fibers, each with a diameter around 2 μm, that were fused at their intersections. As the cells migrated along the described fiber networks, they eventually encountered intersections between two crossing fibers of equal diameter. At these locations, cells were observed to form broad and non-fluctuating protrusions along the fiber surfaces without bias in either fiber direction [46], [47]. On this homogenous fiber diameter system, a cell protruding in a new direction was followed by

the net migration of the entire cell body. Therefore, this initially designed fiber network failed to show protrusions independent from the migratory direction.

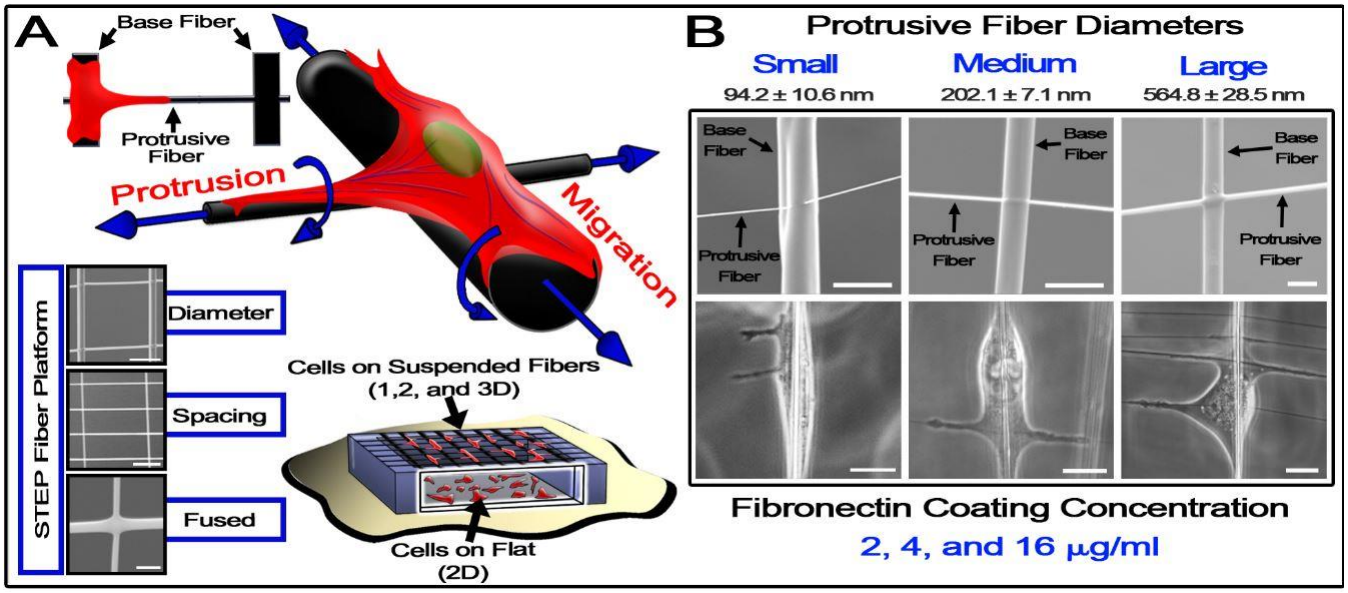

Figure 1. Geometric design of aligned suspended nanofiber networks induce protrusions independent from migration. (A) Schematic illustrating the array of suspended fibers allowing cells to interact with three degrees of freedom: cell body alignment along *base fibers* (1D), protrusion formation and spreading between crossing *base* and *protrusive fibers* (2D), and cell conforming and wrapping around the fiber curvature (3D). Cells were observed to migrate exclusively along the larger *base fibers* while extending protrusions on the perpendicular small diameter *protrusive fibers*. Fibers were created using the Spinneret-based Tunable Engineered Parameters (STEP) technique which allowed for high control of fiber diameter (10 µm scale bar), spacing and alignment (20 µm scale bar), and the fusion of intersections (2 µm scale bar). (B) SEM images of *base fiber* with crossing small, medium, and large diameter *protrusive fibers* (3 µm scale bar). Phase images of cells on the fibers shown below (20 µm scale bars).

In order to successfully separate the protrusion-migration relationship, we varied the fiber diameter within the same assay to introduce geometric disparity between intersecting fibers. Specifically, by producing a network of fibers with a smaller diameter in one direction than in the other, we provided the cells a contrast in fiber curvature and contact surface area. In such an arrangement, large diameter fibers (~2 µm in diameter), denoted as '*base fibers*', served as scaffolding upon which smaller diameter fibers (small: ~100nm, medium: ~200nm and large: ~550 nm) were deposited orthogonally and then fused (Figure 1A). Spacing between *base fibers* averaged 165 ± 29 µm. The smaller '*protrusive fibers'* were observed to elicit pseudopodial

protrusions that exhibited varying temporal and morphological characteristics correlating with the biophysical environment. The bulk of each cell body was situated on the larger *base fiber* and the cells migrated along this direction exclusively. Concurrently, protrusions extended onto the smaller diameter *protrusive fibers* without subsequent migration onto this fiber (Figure 1B). Protrusions were not preferentially formed on a certain side of the *base fibers* or at specific locations relative to the cell body and/or nucleus. The protrusions observed on this fiber network were morphologically distinct from those seen on a flat surface and were clearly distinct from the rest of the cell and its migratory path (Figure 2).

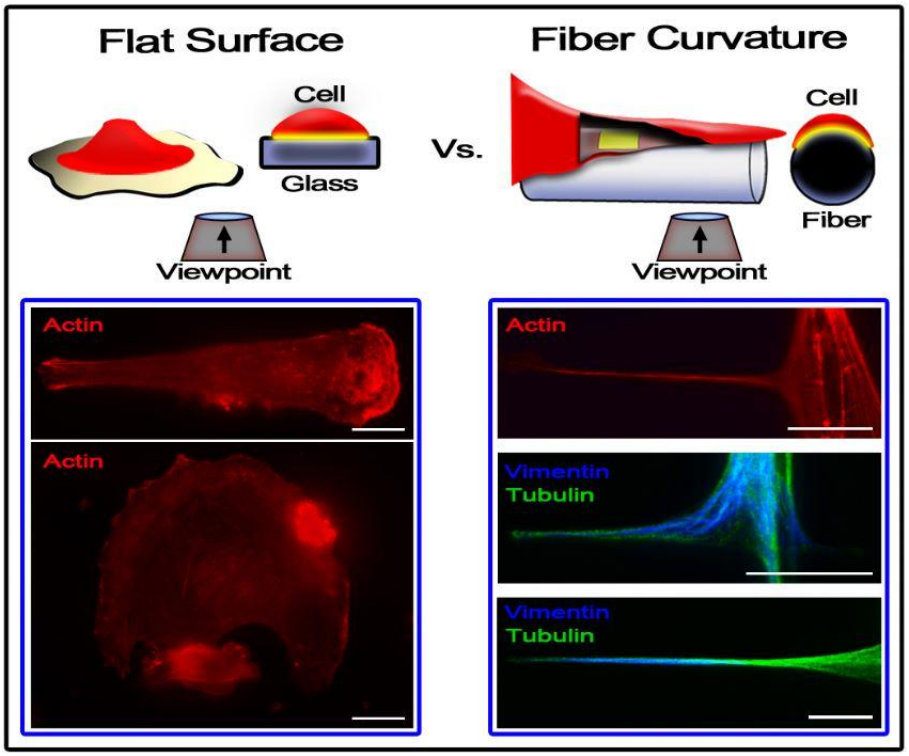

Figure 2. Fiber curvature induces morphologically different protrusions than seen on flat surfaces. On the fiber networks we used, protrusions are elongated along the smaller *protrusive fibers* while the cell body is on the larger *base fiber* (20 µm scale bars).

3.2 Cell protrusions are differentially regulated in response to fiber curvature.

When interacting with *protrusive fibers* of varying curvatures, cells were found to modulate their response as evidenced by the differences observed in maximum protrusion length, base

length, extension rate, and retraction rate (Figure 3A). We defined the maximum length of the protrusion to be the longest distance the protrusion extended away from the main cell body. On the other hand, the base length is defined as the distance the body of the cell moved away from the *base fiber* onto the *protrusive fiber*. For both cell types, these metrics were compared between all three *protrusive fiber* diameters by measuring protrusion features over time (Figure 3B). Also, in order to investigate the role of ligand density and attachment on protrusion dynamics, the protrusions were also studied on varying fiber coating concentrations of fibronectin (2, 4, and 16 µg/ml).

The influence that fiber properties had on the protrusions was clearly apparent due to the distinct characteristics observed between samples (Figure 3C). For both MDA-MB-231 and DBTRG-05MG cells, larger fiber diameters induced protrusion lengths that were significantly longer than those seen on the small diameter fibers (Figure 3D). Also, an increase of fibronectin resulted in significantly longer protrusion lengths for MDA-MB-231 for all three diameters, however, it only increased the protrusion lengths for DBTRG-05MG on the small diameter fibers. Overall, DBTRG-05MG extended longer protrusions than MDA-MB-231 on large diameter ($p<0.01$), medium diameter ($p<0.05$), and small diameter fibers ($p<0.001$). On average, DBTRG-05MG formed protrusions with lengths that generally ranged between 20 to 25 µm throughout. In comparison, the average protrusion lengths of MDA-MB-231 were more widespread due to a higher dependence on fiber diameter and fibronectin coating. As the concentration of fibronectin was raised from 2 to 16 µg/ml, the corresponding protrusion length averages were: 13 to 18 µm on small diameter, 18 to 23 µm on medium diameter, and 20 to 25 µm on large diameter fibers. The base lengths of the two cell types typically increased with fibronectin concentration but not with fiber diameter. Also common between these cell types, extension rates were generally seen

to vary between 2 to 3 µm/min while retraction rates were relatively faster and ranged from 4 to 7 µm/min.

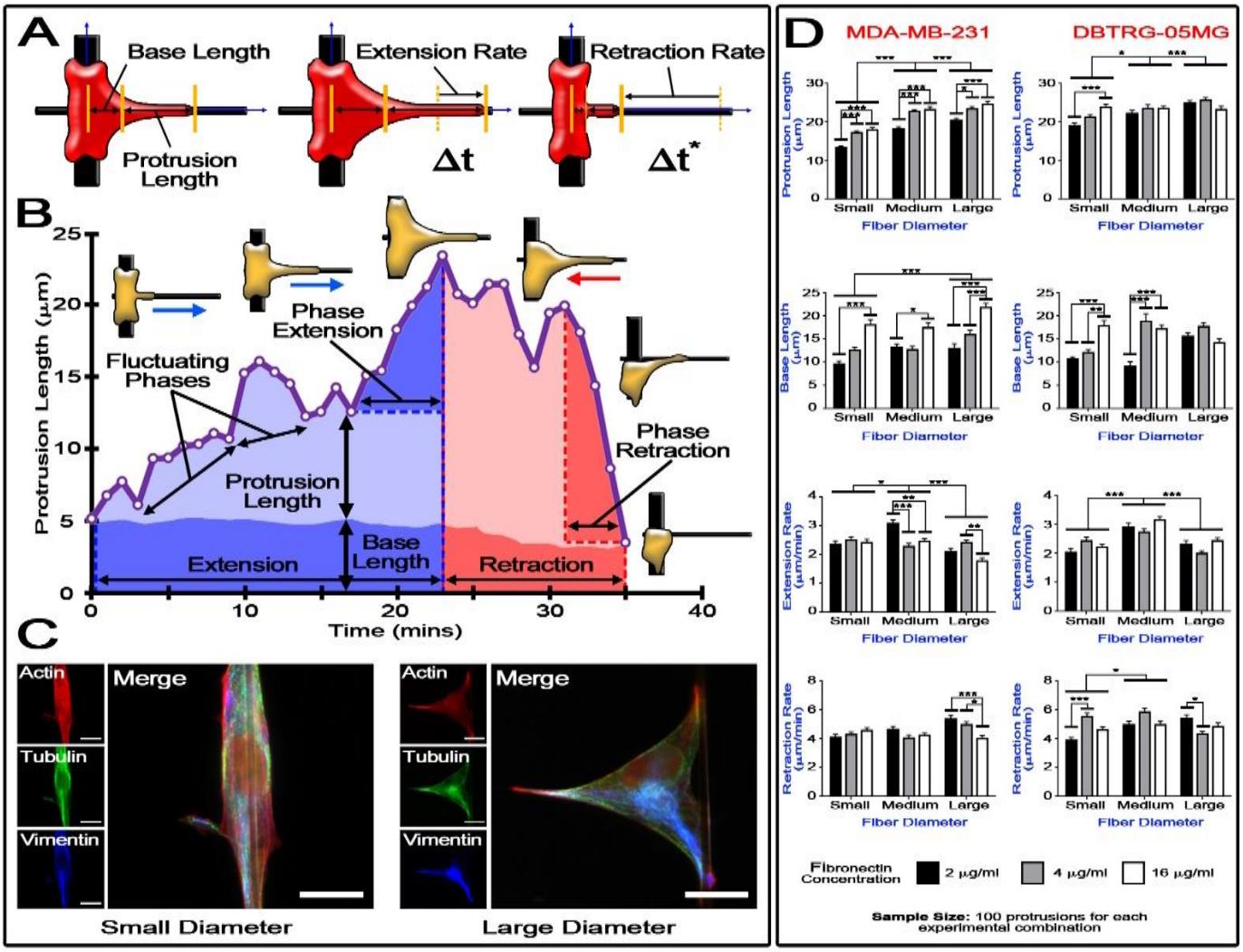

Figure 3. Protrusion length, base length, and extension and retraction rates are influenced by fiber diameter and fibronectin coating concentration. (A) Schematic illustrating the metrics measured were protrusion length, cell body length, extension rate, and retraction rate. (B) A representative protrusion profile showing protrusion maturation over time in minutes. The profile is segmented into elongation and retraction time periods with additional metrics annotated. (C) Immunofluorescent images of cells on small diameter (left) and large diameter (right) fibers (Scale bars are 20 µm). (D) For MDA-MB-231 (left column) and DBTRG-05MG (right column), protrusion length is highly dependent on fiber diameter and fibronectin concentration, however, fiber properties did not show a major influence on the cell body length, extension rate, and retraction rate (n=100 per test category).

The analyses of these two types of metastatic cells reveal similar trends in protrusion dynamics with MDA-MB-231 to be more sensitive to increase in fiber curvature and fibronectin

concentration compared to DBTRG-05MG. To investigate whether the protrusive dynamics observed is unique to metastatic cells, we compared the protrusions of MDA-MB-231 to those of MCF-10A, which are healthy breast epithelial cells. The comparison study (diameter: small and large, fibronectin concentration: 2 and 16 µg/ml) showed a remarkably higher protrusion length for MDA-MB-231 on both fiber diameters and fibronectin concentrations except for small diameters coated with 2 µg/ml fibronectin (Figure 4). Therefore, an increased protrusion length may be indicative of the metastatic capacity of a cell. However, differences in the base length, extension rate, and retraction rate were not significant, therefore, we suggest that these parameters might play a smaller role in tumor progression.

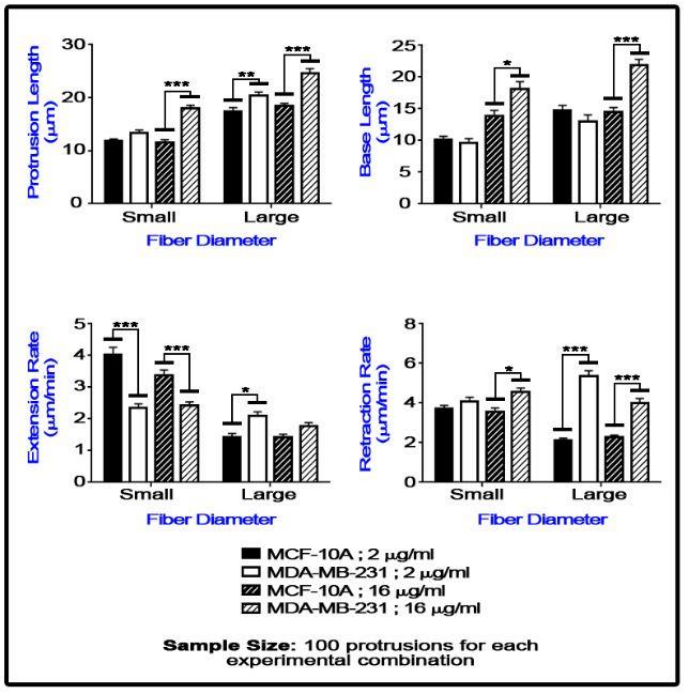

Figure 4. Protrusion length, base length, extension rate, and retraction rate of protrusions compared between MDA-MB-231 and MCF-10A (n=100 protrusions for each test category).

3.3 Protrusion morphology is directly influenced by fiber curvature and is linked to cytoskeletal composition.

The morphology of the protrusion was also investigated since it can provide insights into cell commitment towards migration and the associated structural composition of the protrusion. We noticed that the cell body had different curvatures at the *protrusive-base fiber* interface from which the protrusion was extending and this membrane curvature varied between the cell types and fiber diameters used in the study. In order to quantify the morphological contribution to protrusive ability, we approximated the curvature by fitting an ellipse that outlines the curvature of the cell body and then determined the contributions of its major and minor axis to the ellipsoid shape. Specifically, we calculated the eccentricity (E) of the ellipse, which is a measure of how a morphological curvature of the protrusion deviates from a circle, where a value of zero is a perfect circle and a value of one is straight line (Figure 5A). Protrusions with a low eccentricity were observed to be shorter in length and more rod-like in shape in contrast to protrusions with a higher eccentricity which were more sheet-like and extended further. Generally, protrusions initiated with a low eccentricity and then matured through increase in eccentricity over time.

To compare between cell types and fiber curvatures, we measured the eccentricity at the point when the protrusion reached its maximum length. For MDA-MB-231 cells, the eccentricity dramatically increased in response to increasing fiber diameters. The average eccentricities on the large diameter fibers ranged from 0.86-0.89 (sheet-like) whereas a lower range of 0.60-0.72 (rod-like) was observed for the small diameter fibers. The protrusions seen on medium diameter fibers had eccentricities between 0.70- 0.82 with an intermediate morphology between rod and sheet-like forms. The DBTRG-05MG cells showed sheet-like protrusions with high eccentricities on the

large diameter fibers (0.80-0.83), however, narrower protrusions were observed on medium and small diameter fibers which resulted in lower eccentricities between 0.70- 0.74.

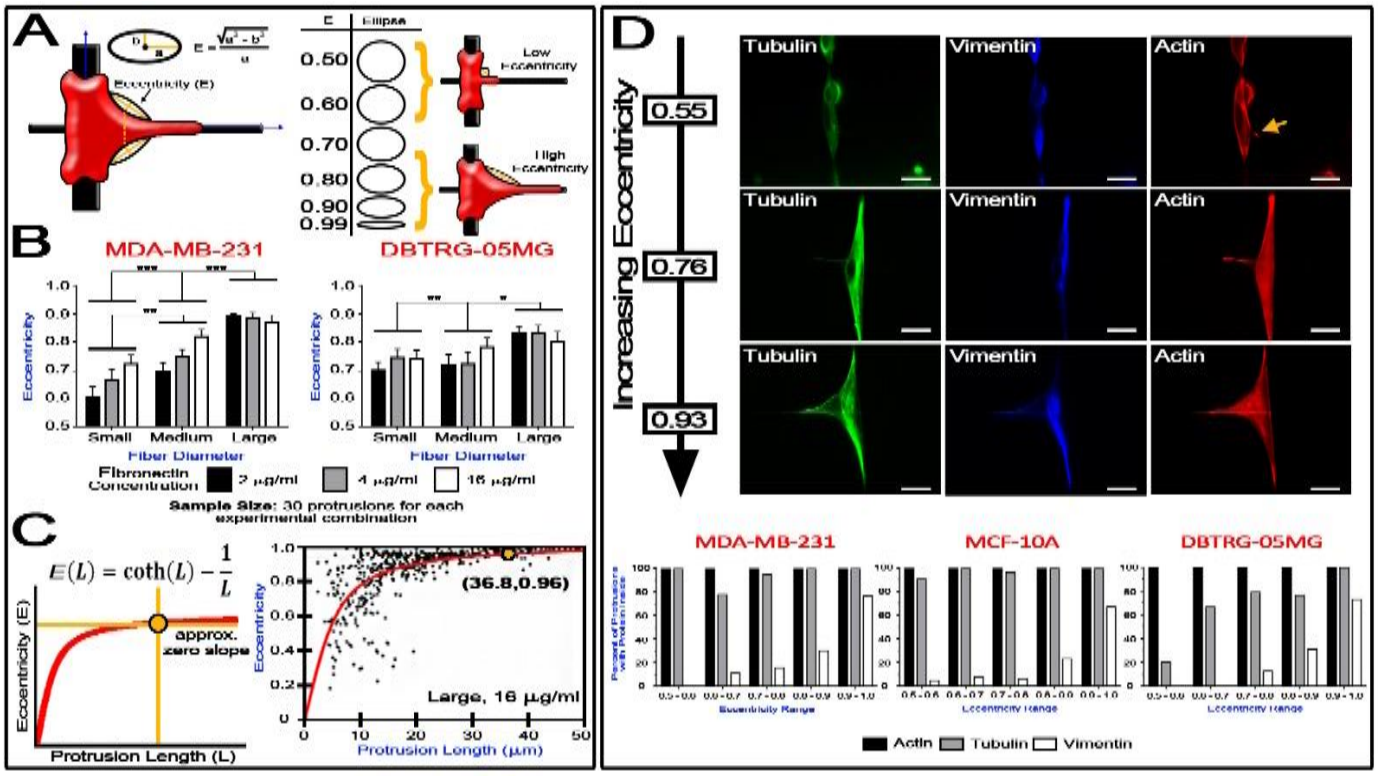

Figure 5. The quantification of protrusion morphology with a value of eccentricity relates morphology with fiber curvature and cytoskeletal composition. (A) Eccentricity is found by fitting an ellipse along the curved cell body at the base of the protrusion. Small values of eccentricity denote rod-like protrusions while large values represent sheet-like protrusions. (B) Eccentricity increases with fiber diameter but no statistical significant difference was found due to fibronectin concentration (n=30 per test category). (C) Eccentricity was also found to be a function of protrusion length on a given fiber diameter. The relationship is fitted with a Langevin function curve and the coordinates shown locates the point where the slope approximates zero, indicating the morphology is stable. Graph is shown for DBTRG-05MG on large diameter fiber with 16 µg/ml fibronectin concentration (D) Immunofluorescent images for tubulin (green), vimentin (blue), and actin (red) at three eccentricity values. Vimentin only co-localizes with tubulin at high eccentricities (bottom images) (Scale bars are 20 µm). For each eccentricity range, the bar plot shows the percentage of protrusions that internally show the presence of each cytoskeletal protein (actin, tubulin, vimentin) from fixed cell samples.

Altogether, MDA-MB-231 cells showed a very high dependence on fiber diameter when regulating their protrusion morphology while DBTRG-05MG displayed a more constant morphology except for on the large diameter fibers. For both cell types, the concentration of fibronectin did not have a statistically significant effect on the eccentricity of the protrusions.

Comparing the two cell types, MDA-MB-231 averaged a lower eccentricity on small diameter fibers than DBTRG-05MG ($p<0.05$). Oppositely, on large diameter fibers, MDA-MB-231 had larger eccentricities than DBTRG-05MG ($p<0.01$) (Figure 5B). The fact that eccentricity is positively correlated with the *protrusive fiber* diameter suggests that larger diameters may increase the propensity to initiate migration along the *protrusive fibers*.

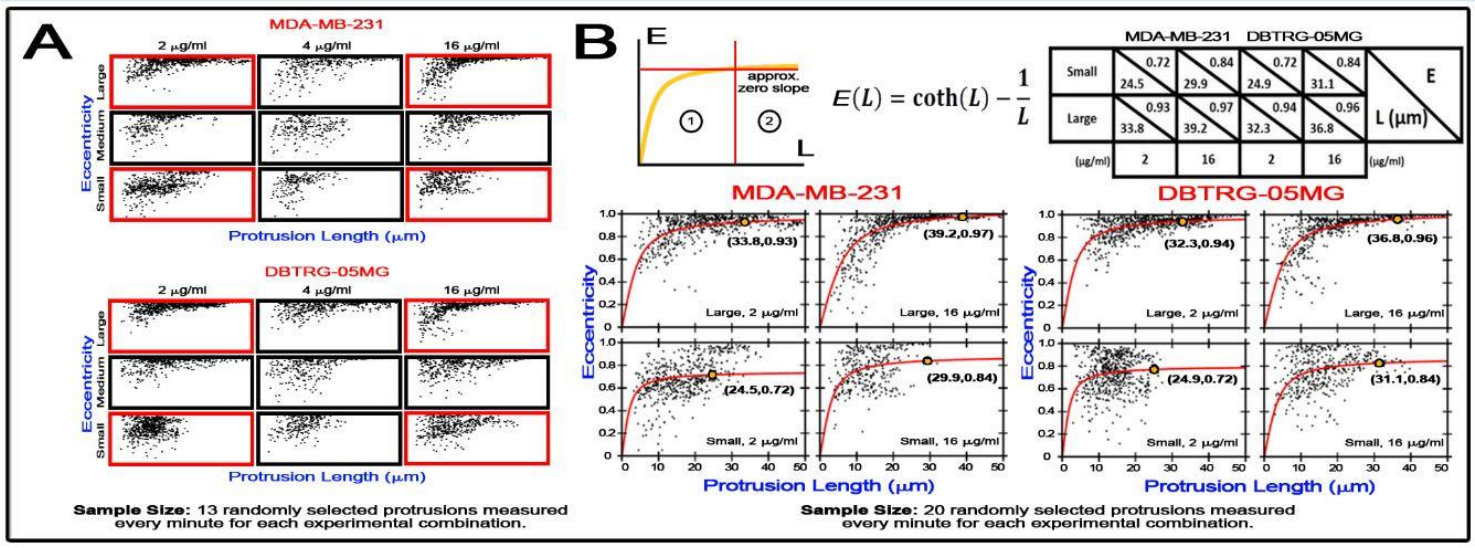

Figure 6. Eccentricity increases with protrusion length up until a certain length, then, eccentricity levels out, or stabilizes.(C) Eccentricity-protrusion length relationships for (i) all test combinations (n= 13 protrusions per test category) and (ii) four chosen test combinations (n= 20 protrusions per test category). The relationship fits a Langevin function curve and the coordinates in the table represent the location where the slope nears zero, indicating stable morphology at the cell population level.

To reveal how the peak eccentricity was obtained, we investigated how eccentricity developed and its association to protrusion length (Figure 5C). For all cases, we found eccentricity to be positively correlated with protrusion length. Newly formed protrusions initially had a low eccentricity that then increased as the protrusion elongated until a maximum eccentricity was reached. When the protrusions continued to lengthen after reaching this maximum, the eccentricity would remain stable at this peak value. The eccentricity-length relationship was found to follow a Langevin function fit, where the eccentricity asymptotically approached values of 0.9 or higher as length increased. The coordinates on the fitted curve where the slope approximates zero represent

the length at which the growth of eccentricity ceases. We found that coordinate values increased with fiber diameter and fibronectin concentration (Figure 6).

The fact that the protrusions are rich in actin can be inferred from the long lengths and broad morphologies achieved, however, the extent in which microtubules and intermediate filaments are involved is not as obvious. Through fixed immunostaining, we investigated the presence of actin, tubulin, and vimentin within protrusions of varying eccentricity (Figure 5D). As expected, the rhodamine phalloidin marker was always visible throughout the entire protrusion which supports our initial inference of an actin-rich structure for both high and low values of eccentricity. Although not as prevalent as actin, localization of tubulin (microtubules) was also observed at low (~20%-60% occurrence) and high (~75%-100% occurrence) eccentricities. Contrarily, vimentin intermediate filaments were rarely detected within protrusions with eccentricities below 0.75. However, the percentage of protrusions positively marked with vimentin increased as eccentricity increased and it reached a maximum occurrence of 73% at eccentricities between 0.90 and 1.00. Overall, the presence of vimentin within protrusions is highly linked to the protrusion morphology, whereas, tubulin was present at least 20% of the time regardless of the eccentricity. When vimentin and tubulin were both observed, their distribution and concentration throughout the protrusion appeared to match which is indicative of them being bundled collinearly.

3.4 Protrusions underwent fluctuating extension and retraction phases as the overall net protrusion length increased.

Protrusions were not observed to extend continuously. Instead, protrusion lengths would fluctuate as they elongated along the *protrusive fiber*. We denote the first extension and retraction as the ‘initial phase’. Subsequent ‘fluctuating phases’ would then start with extension occurring after the first phase retraction. Eventually, fluctuation would cease and the ‘final phase’ would

begin resulting in the termination of the protrusion, which is defined as the cell retracting the entire protrusion back into the cell body (Figure 7A). We observed that on average, fluctuation consisted of 3 phases for MDA-MB-231 and 4 phases for DBTRG-05MG until the protrusion was terminated.

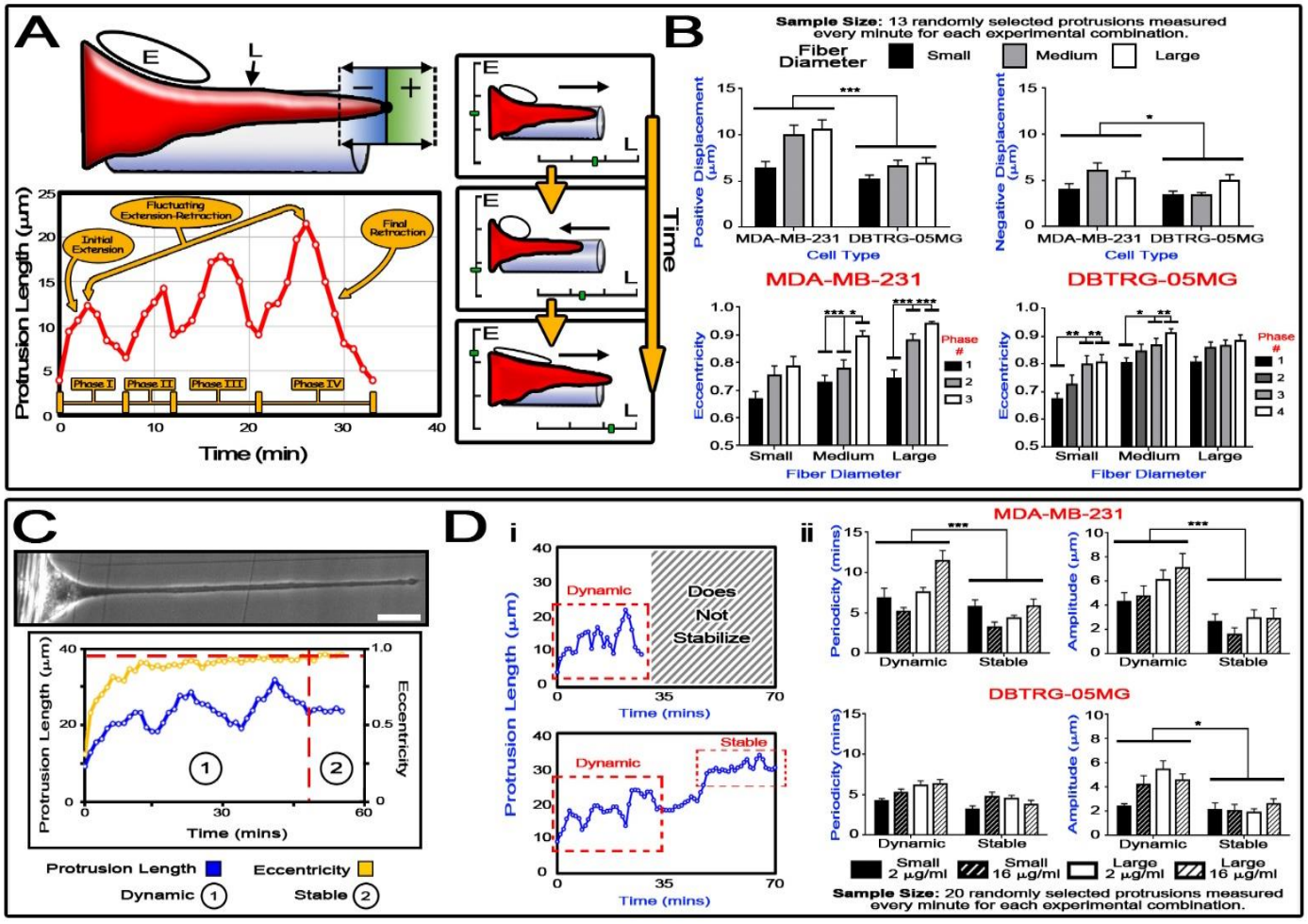

Figure 7. Protrusion elongation was not persistent due the cyclic periods of extension and retraction which only ceased when the protrusion gained a stable morphology. (A) Protrusions fluctuate with positive displacement away from the *base fiber* and with negative displacement towards the *base fiber*. A fluctuating protrusive profile is shown for MDA-MB-231. (B) Positive and negative displacement on small, medium, and large fiber diameters for MDA-MB-231 and DBTRG-05MG. Eccentricity is compared between each extension phase for both cell types. (C) Protrusions show either a dynamic or stable state depending on the degree of length fluctuations and eccentricity of the protrusion (Scale bar 20 μm). (D) (i) Protrusion profiles exhibiting dynamic fluctuations (top) and a stable final length (bottom). (ii) Periodicity and amplitude of the protrusion is compared for each dynamic and stable situations for both cell types. (n= 20 protrusions per test category).

During the cyclic periods of extension and retraction, substantial distances were displaced (Figure 7B). As a result of tracking fluctuating protrusion lengths at one minute intervals, we found

that MDA-MB-231 displaced larger distances (extension: 6-11 µm, retraction: 4-6 µm) than DBTRG-05MG (extension: 5-7 µm, retraction: 3-5 µm). These displacements were not significantly influenced by the fiber diameter or the concentration of fibronectin. To determine if the fluctuations alter the protrusion morphology, we investigated how eccentricity was related to the phase number. Comprehensively, our findings demonstrate that the eccentricity increases as the phase number is incremented. On average, the eccentricity increased by 0.08 per phase for MDA-MB-231 and by 0.04 per phase for DBTRG-05MG. Note that the distances displaced during periods of extension were found to be greater than those displaced during retraction, therefore, the protrusion tip advances away from the *base fiber* over time, despite the periods of retraction.

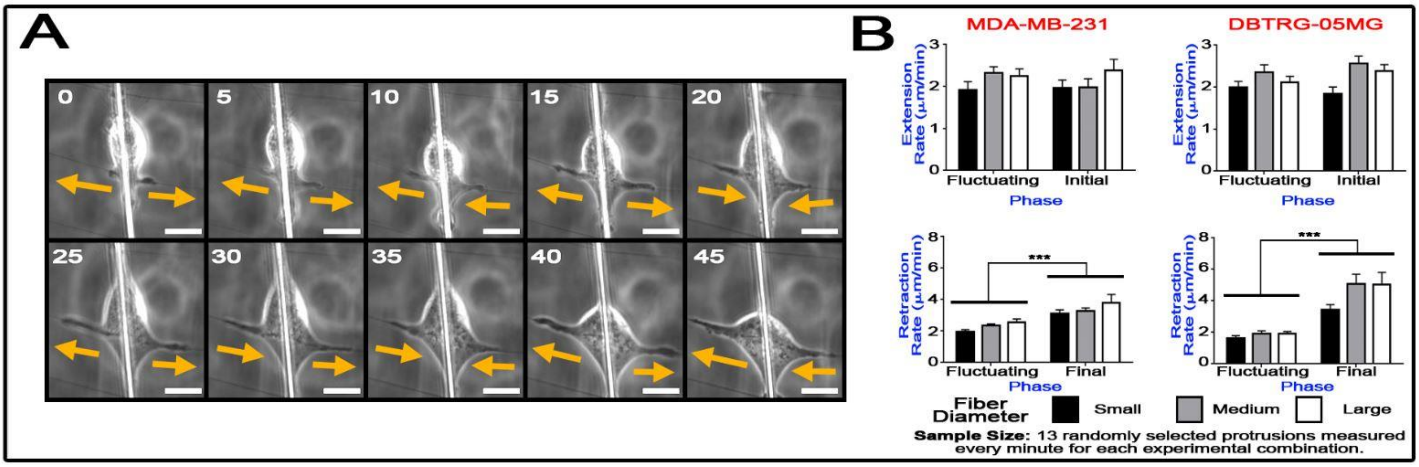

Figure 8. The protrusion length fluctuates during protrusion elongation. (C) Time lapse phase images of cell protrusions with fluctuating lengths. The arrows indicate the direction each protrusion is moving. Scale bars are 20 µm. (D) Extension rate remained constant throughout protrusion while final retraction rate was faster than retraction during fluctuation. (n= 13 protrusions per test category).

Lastly, in order to identify if the temporal dynamics also change throughout a protrusions life, from its formation up till its termination, we investigated how extension and retraction rates varied between the initial, fluctuating, and final phases (Figure 8). Our results show that the extension rate for both the initial phase and the fluctuating phases ranged from 2 to 3 µm/min, which is in agreement with the overall average extension rate reported earlier. However, the final

retraction rate, ranging from 3 to 6 μm/min, was significantly faster than the 1 to 3 μm/min retraction that was observed during fluctuating phases.

3.5 Dynamic fluctuations ceased when protrusion morphology stabilized.

We noticed that the morphology of the protrusion, denoted by the eccentricity, was very dynamic at lower lengths while it became more stable as the length increased (Figure 7C). Here, dynamic behavior describes a rapidly changing morphology with continuous fluctuations of protrusion length that displace large amplitudes. Stable behavior, however, is achieved when the morphology becomes constant and is associated with infrequent fluctuations with smaller amplitudes (Figure 7D(i)). Protrusions were only observed to become stable less than 10% of the time while the majority terminated. We investigated how the protrusions differed, both spatially and temporally, when the protrusions were maturing (dynamic morphology) compared to fully mature protrusions (stable morphology). We looked at the periodicity and amplitude of protrusion length fluctuations within both dynamic and stable cases in order to probe these differences (Figure 7D(ii)). For dynamic behavior, the periodicity of fluctuations ranged from 3 to 12 minutes for MDA-MB-231 and from 3 to 6 minutes for DBTRG-05MG. In the case that protrusions became stable, the periodicity for MDA-MB-231 decreased to be within the range of 3 to 6 minutes while no change was observed for DBTRG-05MG. However, both cell types showed a decrease in amplitude of fluctuation when a stable eccentricity was achieved. When dynamic, the amplitude of fluctuation was seen to be between 3 and 8 μm, however, when stabilized, the average amplitude decreased to around 2 μm for both cell types.

3.6 Cells interacting with multiple fibers show both random and biased protrusions.

Both cell types are able to form multiple protrusions in different directions, sequentially and/or simultaneously, when in contact with more than one *protrusive fiber*. The protrusion's

observed behavior and coordination is interrelated to the migratory state of the cell. The migratory state of the cell is high when the cell frequently passes *base-protrusive fiber* intersections while moving along the *base fiber*, whereas, the migratory state is low when the cell rarely traverses these intersections and remains almost stationary along the *base fiber*. Relative to the *base fiber* direction, a 'stationary' cell body is correlated with 'random' protrusions whereas a 'migratory' cell body is associated with 'biased' protrusions (Figure 9A). Cells displaying randomly directed protrusions extended multiple protrusions outwards onto almost every *protrusive fiber* that they were interacting with while being in a nearly stationary migratory state. Cells displaying this behavior were also seen to simultaneously extend protrusions on opposite sides of the *base fiber* as well as on multiple *protrusive fibers* located along the cell length. The protrusive profile depicting this low migratory mode does not clearly link the direction and location of one or multiple extending protrusions to a particular region on the cell periphery (Figure 9B(i)). This behavior suggests the cell is primarily using its protrusions as a sensory mechanism, carried out by random probing from all sides, while having minimal migration along the *base fiber*.

In contrast, when the cell is in a high migratory state, protrusions primarily form at the leading edge which displays a bias towards the direction of migration. A profile exhibiting biased protrusion behavior clearly shows that protrusion extension favors the migration direction (Figure 9B(ii)). Both the persistent migration along the *base fiber* and the minimal protrusion re-formation on already encountered *protrusive fiber* locations characterizes the biased phenotype observed

here. Both cancer cell types were seen to switch between random and biased protrusions, on minute to hour timescales, when interacting with the nanofiber networks.

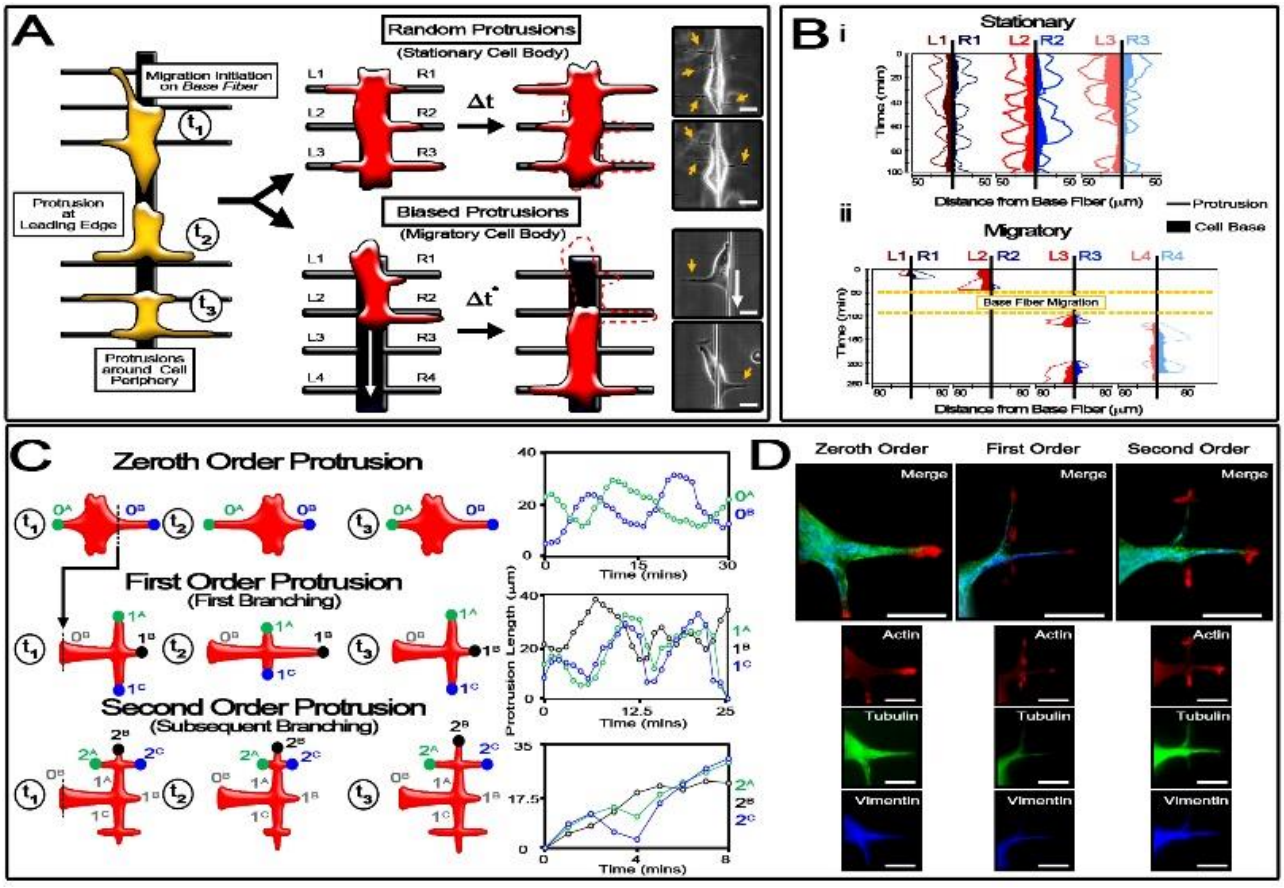

Figure 9. Cells interacting with multiple fibers display random or biased coordination of protrusions while a single protrusions interacting with multiple fibers forms and coordinates protrusion branches. (A) As cells migrate along the fiber networks, they either (i) randomly sense their environment by forming protrusion along all sides of the cell body or (ii) bias their protrusions towards the direction of migration in a coordinated fashion. (B) Protrusion profiles for (i) random and (ii) biased protrusion phenotypes. (C) The original zeroth order protrusion branches into smaller first order protrusions. These protrusion subsets can then branch further into second order protrusions. The first and second order protrusions are all coordinated with one another as shown by the transient plots to the right. (D) Immunofluorescent imaging for zeroth, first, and second order branched structures. Images show actin (red), vimentin (blue), and tubulin (green). All scale bars are 20 μm.

3.7 Individual protrusions interacting with multiple fibers form branched structures.

After looking at how the entire cell responds to multiple fibers, we then investigated how an individual protrusion behaves when it contacts multiple fibers, such as when it reaches a fiber intersection. In order to allow a protrusion to reach an intersection, we added additional fibers

(~200 nm) parallel to the *base fibers.* As a result, protrusions extending along the *protrusive fiber* were observed to branch into multiple smaller protrusions when this additional fiber was encountered. We classified this behavior by calling the initial originating protrusion the zeroth order protrusion. Then, the first set of protrusions that branch from the original are the first order protrusions. On rare occasion, we even saw short-lived structures branch from the first order protrusions, which we call the second order protrusions (Figure 9C). The cytoskeletal composition within each branched protrusion varied. However, we only observed actin within second order protrusions due to the low eccentricities of the captured occurrences (Figure 9D).

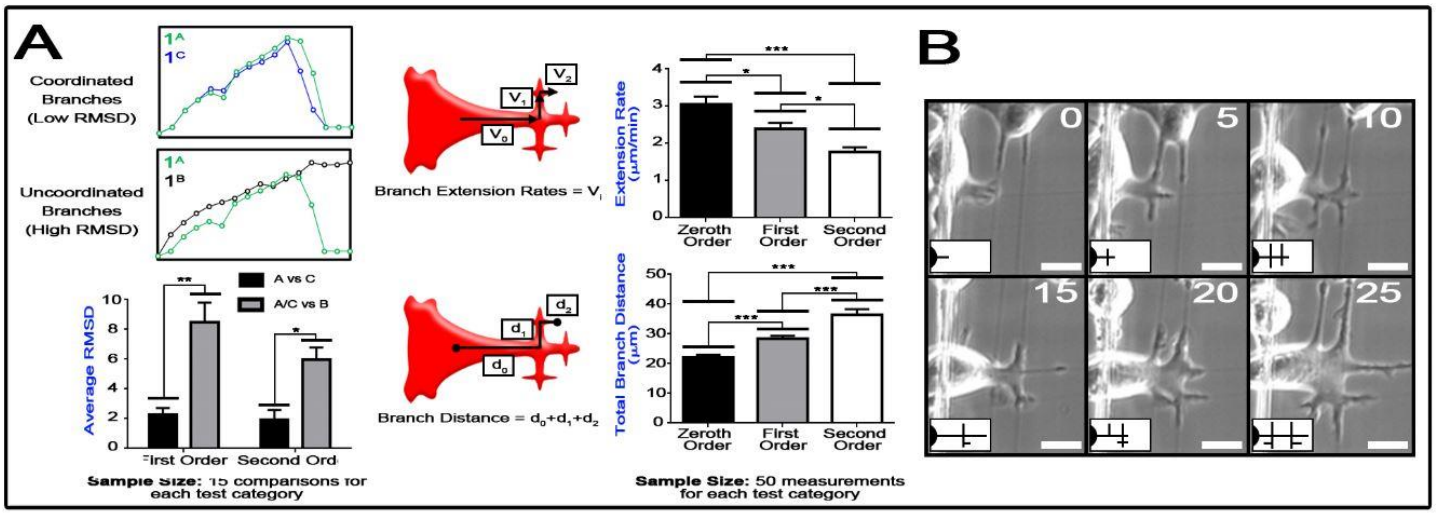

Figure 10. The quantification of the coordination between branches, branch extension rate, and overall branch distance. (A) RMSD measurements shows that protrusion branches are coordinated with one another but not with their originating protrusion (n=15 protrusions). Also, protrusion branches extend slower, however, they allow for more protrusion to be extended outwards onto the fibers (n=50). (B) Protrusion branching time lapse phase images showing complex branching behavior. Time is in minutes and scale bars are 20 μm.

The dynamics of the branched protrusions appear to be coordinated, where branches on opposite sides were at times observed to extend and retract synchronously. However, side branches showed little coordination with branches parallel to the originating zeroth order protrusion. We quantified this by determining the root-mean-square-deviation (RMSD) between transient protrusion length plots (Figure 10A). Results showed lower RMSD values between side branches,

indicating high coordination, while higher RMSD values, indicating low coordination, were calculated between branches perpendicular to one another. Also, we noticed that the protrusions extend at a slower rate as subsequent branching occurs. However, branching allows more protrusion to be extruded outwards on the fiber, away from the cell body. The branched structures can also form very complex arrangements when protrusions interact with multiple crossing fibers in which numerous branched protrusions are assembled and disassembled (Figure 10B).

3.8 Protrusion fragments are deposited on fibers by maintaining attachment at the tip during final retraction.

For both MDA-MB-231 and DBTRG-05MG cell lines, we also observed protrusion fragments being deposited on fibers and, at times, collected by other cells (Figure 11A). Although the fragments varied in shape and size, they were seen to be either spherical (5 to 25 μm in diameter) or elongated narrow cylinders (10 to 40 μm in length). Most fragments remained stationary at the location they were placed and continuously altered their shape. In certain instances, protrusion fragments were also observed to translate autonomously across the fibers (~1.4 μm/min).

Protrusion fragments were seen to be deposited on the fibers through a multi-step process (Figure 11B). First, the protrusion extending on the *protrusive fiber* would start to show large balloon-like ruffles emerging at the tip which then moved rearward along the protrusion's length to the base. Second, the ruffles would persist until the cell initiated migration along the *base fiber* while still maintaining attachment of the protrusion tip on the *protrusive fiber* (Figure 11C). As the cell continued to move away, the protrusion would narrow due to necking. Third, the narrowed protrusion eventually failed, thus, leaving the still-attached protrusion tip on the *protrusive fiber*

in the form of a cellular fragment. Other cells have been seen to migrate to the location of the fragments, extend a protrusion to grab it, and then retract in order to assimilate the material.

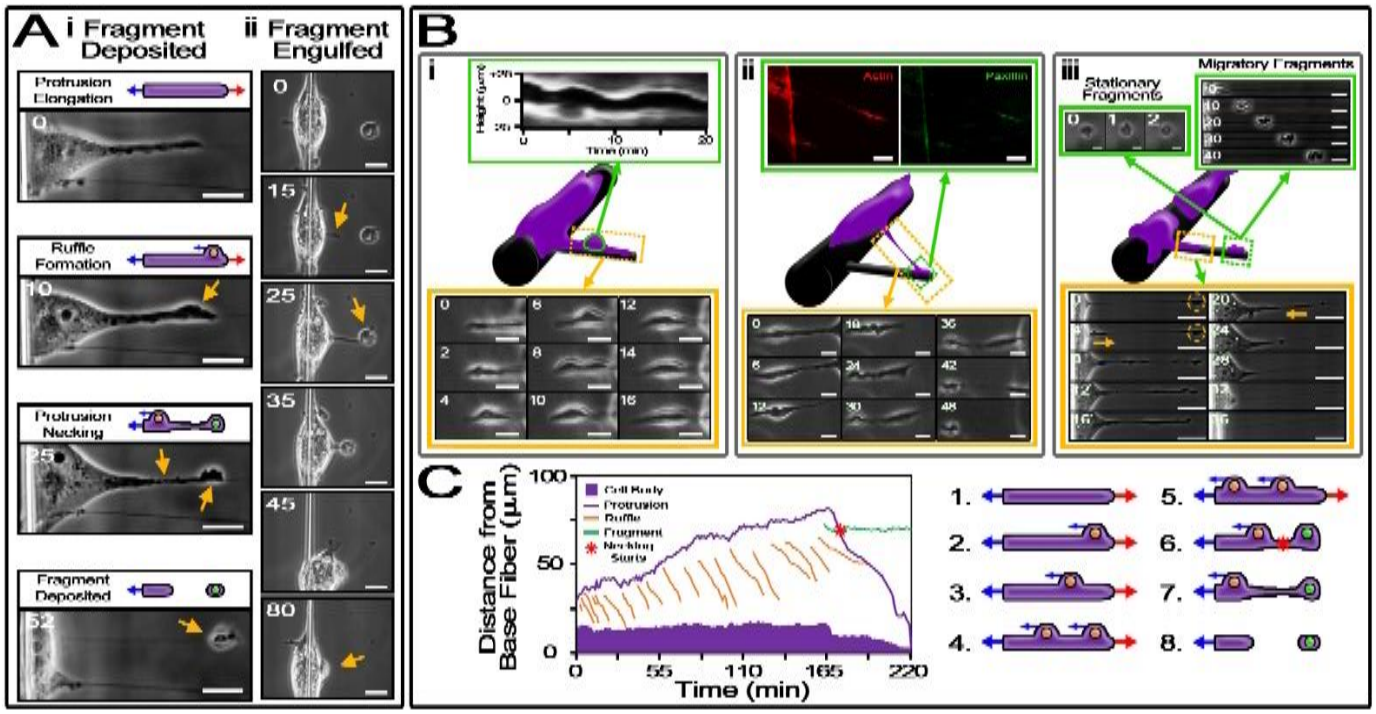

Figure 11. Cells use protrusions to leave and collect cellular fragments at locations away from their migratory path. (A) Cells can either (i) create protrusion fragments or (ii) grab and engulf protrusion fragments. Scale bars are 20 µm. (B) Protrusion fragments are created in a three step process where first (i) bulges/ruffles appear along the protrusion periphery (Scale bars 5 µm). (ii) The cell then begins to retract while maintaining attachment at the protrusion tip. The contractions cause the protrusion to thin due to necking. Scale bars for immunofluorescent images and time lapse frames are 20 µm and 5 µm, respectively. (iii) Finally, the protrusion tip is disconnected from the rest of the protrusion, leaving protrusion fragment on the *protrusive fiber*. The fragments can be stationary (5 µm scale bars) or migrate along the fibers (20 µm scale bars). Time lapse frames (bottom) shows another cell extend a protrusion to grab and assimilate the fragment. (20 µm scale bars). (C) Protrusion profile showing the deposition of a cell fragment (green) occurring during protrusion retraction (purple). A physical interpretation of the plot is shown on the right in illustrated steps.

3.9 Fiber deflctions reveal protrusion contractile force loading and magnitude.

In addition to sensing curvature and surface area, protrusions were observed to deflect the *protrusive fiber* while the cell body migrated along the *base fiber*, signifying that the cells are also sensing the structural stiffness along the fibers. For deflection to occur, cells must exert adequate force onto the fiber. Since the fibers were seen to deflect towards the cell body, these forces are contractile in nature. In order to analyze and measure these forces, the deflecting *protrusive fiber*

was modeled as a cylindrical beam while the non-deflecting *base fibers* served as the beam supports (Figure 12A-i). Previously shown by our lab, the STEP fiber manufacturing process produces fibers with residual axial stress, which means all fibers are in tension. Regardless of the fiber diameter or molecular weight used, the process causes all fibers to have an inherent tensile stress of 4.1 MPa. However, the boundary conditions of the *protrusive fiber*; the load type and magnitude exerted by the cells; and the effects of diameter, tension, and elastic modulus remained unclear.

To examine the effects that the fiber elastic modulus, diameter, and tension has on the deflection of the *protrusive fiber*, we derived a differential equation that describes the deflection of a loaded beam at all locations throughout the fiber length. Using this equation, we used Wolfram Mathematica software to solve the boundary value problem using a numerical technique called the "Shooting Method." Therefore, by changing the model inputs, which represent the physical nature of the system, the effect on the beam deflection was observed (Figure 12A-ii). Changing the flexural rigidity of the fiber, which is the product of the elastic modulus and the moment of inertia, resulted in very little to no change in the modeled fiber deflection. On the other hand, changing the tensile stress, which only impacts the tension of the fiber, significantly effected the fiber deflection where larger deflections were seen at lower tensile stresses, as expected. When the diameter of the fiber was changed, which effects both the flexural rigidity and the tension, the deflection of the beam was significantly effected as well. Therefore, we conclude that fiber deflection is most influenced by tension.

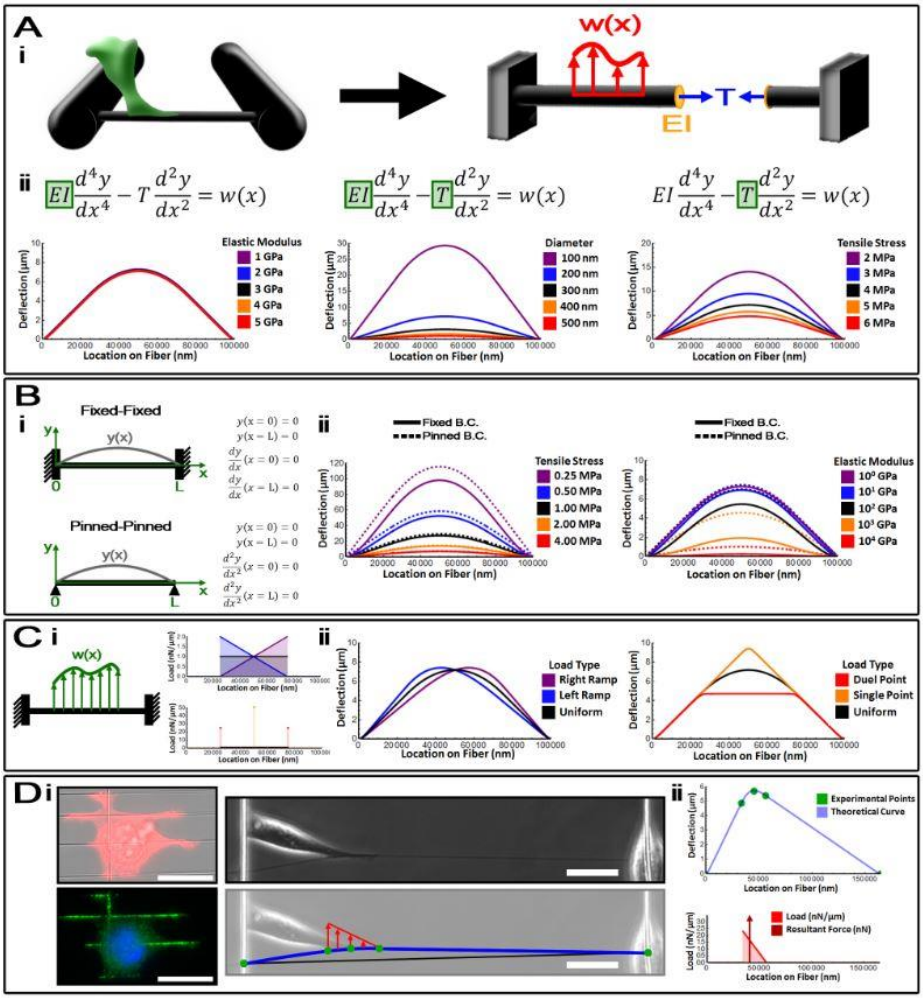

Figure 12. *Protrusive fiber* deflection measurements can be used to calculate protrusion contractile forces. (A) The *protrusive-base fiber* system can be modeled as (i) a cylindrical beam with defined material and geometric properties, tensile residual stress, and loading. (ii) Analysis of the flexural rigidity, fiber diameter, and tensile stress revealed that fiber deflections are most dependent on the tension magnitude. (B) The fiber system is depicted with fixed-fixed boundary conditions, however, a pinned-pinned system would show similar fiber deflections due to the system properties. (C) Single point load, double point load, uniform distributed load, and ramp distributed loads were analyzed and all result in unique fiber deflection profiles. Therefore, the correct load type must be chosen in order to match experimental fiber deflection profiles. (D)

In order to solve the boundary value problem accurately, the proper boundary constraints that define the system must be chosen (Figure 12B-i). Since the fibers were fused at every intersection between the *protrusive fibers* and the *base fibers*, the boundary conditions are fixed-fixed, as opposed to pinned-pinned. However, we modeled both boundary condition types in order to compare and better understand the system. Using the properties of this fiber system, the fiber

deflection curves for both boundary conditions were extremely similar. However, if the tension was reduced or the elastic modulus was increased, the difference between fixed-fixed and pinned-pinned boundary conditions became greater (Figure 12B-ii). Therefore, we conclude that for our system properties, the boundary condition used has little effect, however, the fixed-fixed condition better represents our system due to the fused fiber intersections.

Lastly, we looked at the effects of the type of load in order to develop the proper loading used to model the observed protrusion contractile forces. The load types examined were a single central point load, two distant point loads, a uniform distributed load, and a ramp distributed load (Figure 12C-i). When point loads were modeled, the resulting curve was unsmooth and pointed in appearance. On the other hand, distributed loads resulted in curves that matched the experimental fiber deflection profiles very closely (Figure 12C-ii). Uniform distributed loads resulted in symmetric curves while ramp distributed loads resulted in curves skewed to a particular boundary, depending on the load orientation. Therefore, the type of load used in the model needs to be chosen wisely in order to match experimental fiber curves, and therefore, accurately model the system.

Immunofluorescent imaging revealed that the focal adhesion marker paxillin was distributed across the entire protrusion-fiber interface (Figure 12D-i). Therefore, this interface serves as the region at which the load is applied. Also important to note, the load must be applied towards the cell body, which is located on the *base fiber* either to the left or right of the load. Due to this, the experimentally observed fiber deflection profile is skewed towards the cell body, therefore, a properly oriented ramp distributed load must be used when modeling protrusive contractile forces. A representative case shows that the experimentally measured fiber deflection profile matches the theoretically derived deflection profile perfectly (Figure 12D-ii). From this, the load and resultant force magnitude can be deducted from the load inputs used in the model

when a match is made. For the example shown, the highest ramp load magnitude is 2.3 nN/µm and the resultant force magnitude is 26 nN. Due to the flexibility and capabilities of this model, it serves as a very useful and universal tool to measure cellular forces on this fiber-based systems.

To demonstrate the usefulness of this model for cell biology, we used it to compare the force exertion of MDA-MB-231, MCF-10A, and DBTRG-05MG cell lines at varying stiffness values along the fibers. The overall force-stiffness relationship showed a positive correlation in which higher forces were exerted at higher stiffness values (Figure 13). Cells have been seen to

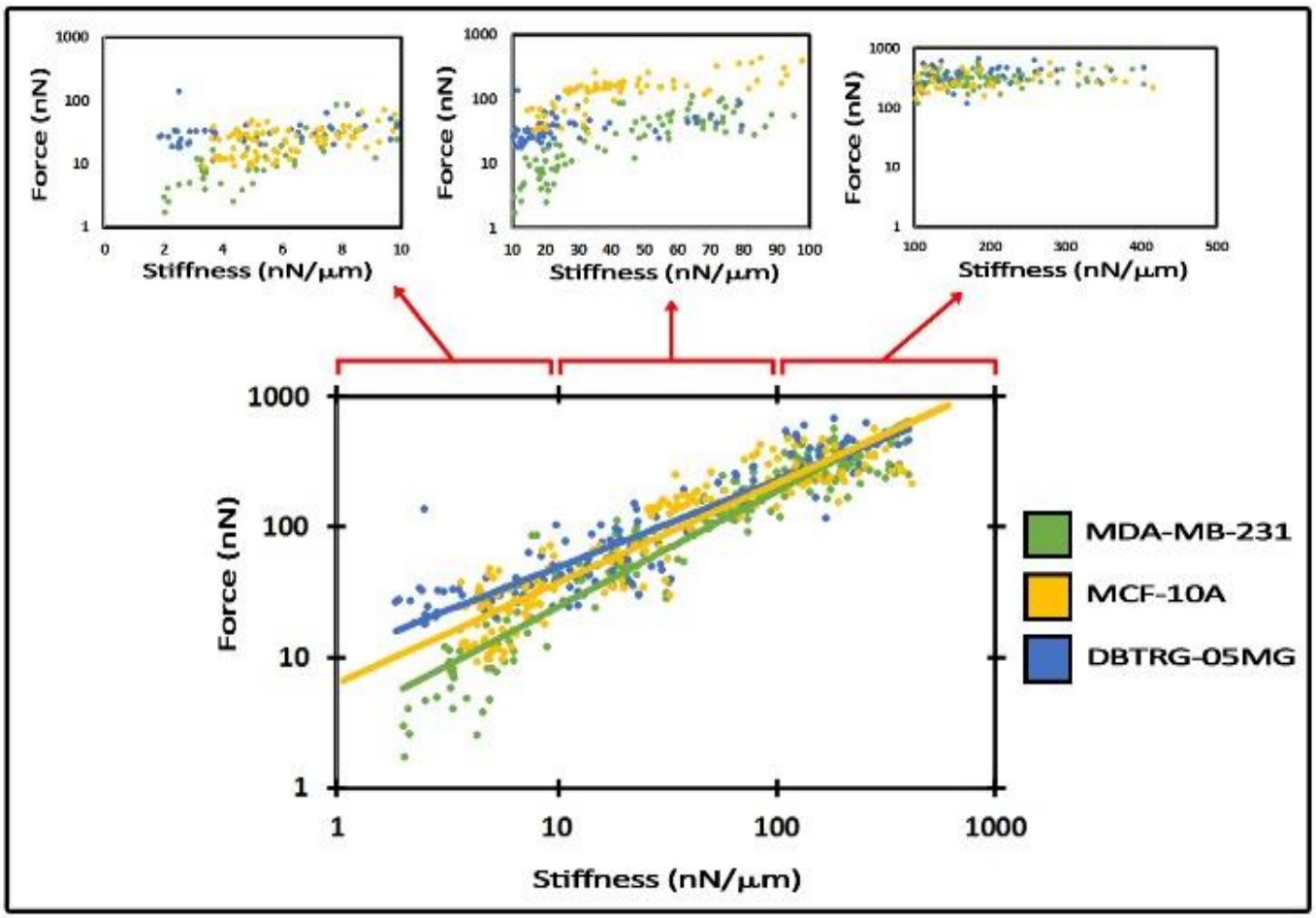

Figure 13. Force comparison between MDA-MB-231, MCF-10A, and DBTRG-05MG at varying stiffness values. The overall force-stiffness relationship shows a positive correlation in which higher forces were exerted at higher stiffness values along the fibers. To analyze the data further, sections of the overall plot were plotted individually to compare force exertion at lower, middle, and higher stiffness values. At lower stiffness values (0-100 nN/µm), force-stiffness relationship is positively correlated and MCF-10A showed slightly higher force values than MDA-MB-231. However, at high stiffness values (100+ nN/µm), the force exertion for all cell types did not increase with stiffnes, signifying a maximum force exertion.

exert high traction forces on flat surface of higher stiffness, however, here, we show cellular force exertion regulated by fiber structural stiffness.

In order to probe the differences between cell types, we looked at specific stiffness ranges. At the lower (1-10 nN/µm) and middle (10-100 nN/µm) stiffness values, MCF-10A normal breast cells showed higher force exertion than their diseased cancerous counterpart, MDA-MB-231. Also, comparing two invasive cancerous cell lines, DBTRG-05MG showed higher force exertion than MDA-MB-231 as well. However, at high stiffness values (100+ nN/µm) the force exertion for all three cell types did not significantly increase with stiffness and force values were seen to be a relatively constant value. Therefore, this indicates an equal maximum force exertion for all three cell lines.

4. DISCUSSION

For breast cancer patients with the poorest prognosis, collagen bundles and fibers are aligned radially to the tumor border and provide a linear path to aid in metastasis [13]. These fibers have been reported to be 70 nm in diameter while bundle sizes ranged from 0.5 to 30 μm [36], [39]. Glioblastoma cells migrate throughout the central nervous system on linear paths as well. For example, they travel on myelinated axons which can be 0.1 to 0.5 μm in diameter or along the periphery of blood vessels where sizes vary widely from a few micrometers to millimeters, depending on location [48]. The nanofiber diameters (~100 nm, 200 nm, 550 nm, and 2 μm) used in this study serve as similar conduits for cell-substrate interactions with respect to size, geometry, and ligand availability. Also, the protrusions we analyzed take place at the interface between large *base fibers* and small *protrusive fibers*. The contrasting fiber properties create geometrical variation that reflect the mechanical heterogeneity present within and around native tumors. Cancer cells often interact with these nonuniform regions and the acclivity or declivity of the gradients contribute to invasiveness. For instance, glioblastoma cell invasion is reported to preferentially take place within mechanically distinct interfaces that are between structures such as blood vessels and white matter tracts [49], [50]. In addition to purely biophysical properties, we also coated the fibers with fibronectin which is native to both breast and neural tissue as well as being significant for metastasis [46], [47], [51]. Therefore, by testing various diameters and fibronectin concentrations, the platform presented in this study addresses the heterogeneity of the tumor microenvironment and probes its effect on cancer cell protrusive behavior.

When examining the protrusion dynamics during extension-retraction fluctuations, we found that the MDA-MB-231 cells displaced much larger distances than DBTRG-05MG in both the positive (outward) and negative (inward) directions. Therefore, since protrusion extension for

DBTRG-05MG is more persistent, it could explain why they averaged overall longer protrusions on all three fiber sizes. The extension rate of protrusion was fairly constant through the entire study which signifies that the duration of time spent extending during the fluctuating phases is directly linked to the maximum protrusion length achieved. Therefore, DBTRG-05MG averaging more phases of extension could also play a role in the slightly longer lengths observed. On the other hand, the final retraction during the termination of a protrusion was much faster than the retraction that took place during fluctuation. This indicates that the cell is still committed to sensing and extending upon the *protrusive fiber* when retracting during the fluctuating phases.

We observed that fluctuation of the protrusion length stopped once a stable morphology was achieved. Protrusions in this state are characterized by a high eccentricity and long length, thus, they contain peak amounts of cytoskeletal proteins. Therefore, stabilized protrusions may be beneficial to the cell when attempting to surpass basement membranes or epithelial layers. On 2D modified Boyden chambers, it has been shown that cancer cells initially extend multiple protrusions into the porous membrane [3], [26]. However, the cell eventually chooses only one protrusion to mature and stabilize, which might be similar to the process we observe on this multi-dimensional fiber platform.

Biased protrusions are characterized by the cell extending coordinated protrusions primarily at the leading edge in order to probe the environment ahead of them in the direction of migration. The protrusions have a short duration since they show minimal fluctuation and the cell migration is more persistent along the *base fiber*. Randomly protruding cells are observed to be virtually stationary at the *base-protrusive fiber* intersections and form protrusions on all fiber locations available, at times simultaneously, without an overall favored direction. This behavior is similar to that seen in fibroblasts where multiple protrusions radiating in different directions

compete with one another, and therefore cause inefficient migration [52]. The random protruding state of the cancer cells on the nanofiber systems also resembles the surveillance mechanisms of microglial cells during their resting state before initiating migration [53].

The high degree of coordination seen between protrusion branches suggests that branching is an important process for migration in fibrous environments. Similarly, branched protrusive structures have been shown to be effective for migration in 3D collagen gels [28]. Branched protrusions in these gels are most likely used to find and/or create porous passageways for migration through either MMP-mediated degradation or traction forces. In contrast, branching on suspended fiber networks serve to transform unidirectional protrusions into structures capable of sensing 1, 2, and 3D dimensionalities due to a single protrusion spreading into multiple higher order protrusions that extend in other directions. Observations between protrusion branches also suggests that the coordination seen may be due to conservation principles.

Both MDA-MB-231 and DBTRG-05MG were shown to deposit and engulf protrusion fragments. Prior to the formation of the fragments, balloon-like bulges appear and move inward along the protrusion length. At times, multiple bulges are present and seem to pump material towards the protrusion tip in a peristaltic-like manner. Overall, the bulges seen on suspended fibers most closely resemble the dorsal ruffles seen on 2D substrates due to their dynamics and morphology. The ruffles may be needed to internalize receptors and other proteins as a preparation for protrusion detachment [54]. The decreased adhesion along the protrusion length, due to the onset of termination, may be responsible for the formation and increase in ruffle magnitude and occurrence [55]. Cancer cells have been known to release high amount of cell fragments which maintain dynamic morphologies and even change locations at low speeds, most likely due to diffusion [56]. In contrast, we see linear movement of detached fragments along fiber conduits for

long distances and at high speeds. Rapid movement of cytoplasmic fragments has been previously reported for fish keratocytes, however, here we show the fragments maintaining attachment to fibers and translating along them [57]. Also, cellular fragments are usually shed from the trailing edge along migration tracks, as seen specifically by MDA-MB-231 in 3D collagen matrices (49, 50). Here, for both cell types, our observations suggest that protrusion fragments are able to be deposited away from the cell body on regions of the fiber that the cell has not migrated on. Therefore, cell fragments may be placed wherever cells are able to protrude instead of only where they are capable of migrating. Immunofluorescent imaging has indicated that the fragments we observed are rich in actin, however, the entire molecular composition is not known. Cancer cells leave cellular material behind as a communication mechanism or guidance cue similar to a 'trail of breadcrumbs' that leads follower cells in the direction of the leader cells during metastasis. The assimilation of the fragments by other cells can even induce certain phenotype changes unachievable by any other means [60].

The inverse mathematical model used to calculate protrusion contractile forces can be used to further address the role of forces in cell protrusion, migration, and ultimately, metastasis. Other groups have attempted to use force measurements as a means to quantify the metastatic capacity of cells, however, not every group is in agreement. One group compared the contractile force of normal cells to a benign L929 cell line and a malignant HeLa cell line using a nanowire array. The contraction forces for the benign and malignant cell types were 50% and 20% greater, respectively, than the normal cell line [61]. However, in disagreement, another group used fibronectin coated hydrogels and measured traction forces that decreased as the metastatic capacity increased [62]. This further proves the importance of having the ability to customize all aspects of a model to the physical system in order to deduct accurate information.

In conclusion, we demonstrated the development of a new suspended and aligned nanofiber platform for studying the formation, maturation, and dissolution of protrusions that are independent from whole cell body migration. Our findings provide new knowledge on how the specific properties of a fiber microenvironment, in this case the fiber curvature, can either promote or inhibit the development of protrusions. The observed effect of fiber diameter on protrusion behavior emphasizes the need to further investigate the role of curvature at nanoscales due to the various surface topographies encountered *in vivo*. Examination of signaling molecules, such as the Rho GTPases, can provide further knowledge on the extent in which these protrusions are initiating migration and at what point during this process does it receive the sensory information that commences protrusion termination or stabilization. Future studies aim to further explain the roles of the mechanical environment on controlling protrusion behavior as well as addressing how active mechanical perturbation and chemical stimulation can influence these processes. The term 'pseudopodia' means "false feet". It is our aim to identify means to disable cancer's 'feet' through first understanding the governing mechanistic relationships that link cancer cell protrusions to sensing and, second, how the mechanotransduction either encourages or suppresses the initiation of migration.

REFERENCES

[1] C. I. Lacayo, Z. Pincus, M. M. VanDuijn, C. a Wilson, D. a Fletcher, F. B. Gertler, A. Mogilner, and J. a Theriot, "Emergence of large-scale cell morphology and movement from local actin filament growth dynamics.," *PLoS biology*, vol. 5, no. 9, p. e233, Sep. 2007.

[2] J. Albuschies and V. Vogel, "The role of filopodia in the recognition of nanotopographies," *Scientific Reports*, vol. 3, Apr. 2013.

[3] M. Schoumacher, D. Louvard, and D. Vignjevic, "Cytoskeleton networks in basement membrane transmigration.," *European journal of cell biology*, vol. 90, no. 2–3, pp. 93–9, 2011.

[4] K. Wolf, M. Te Lindert, M. Krause, S. Alexander, J. Te Riet, A. L. Willis, R. M. Hoffman, C. G. Figdor, S. J. Weiss, and P. Friedl, "Physical limits of cell migration: control by ECM space and nuclear deformation and tuning by proteolysis and traction force.," *The Journal of cell biology*, vol. 201, no. 7, pp. 1069–84, Jun. 2013.

[5] R. J. Petrie, N. Gavara, R. S. Chadwick, and K. M. Yamada, "Nonpolarized signaling reveals two distinct modes of 3D cell migration.," *The Journal of cell biology*, vol. 197, no. 3, pp. 439–55, Apr. 2012.

[6] G. T. Charras, J. C. Yarrow, M. a Horton, L. Mahadevan, and T. J. Mitchison, "Non-equilibration of hydrostatic pressure in blebbing cells.," *Nature*, vol. 435, no. 7040, pp. 365–9, May 2005.

[7] D. Hanahan and R. a Weinberg, "Hallmarks of cancer: the next generation.," *Cell*, vol. 144, no. 5, pp. 646–74, Mar. 2011.

[8] D. N. Louis, "Molecular pathology of malignant gliomas.," *Annual review of pathology*, vol. 1, pp. 97–117, Jan. 2006.

[9] M. W. Conklin and P. J. Keely, "Why the stroma matters in breast cancer," *Cell adhesion & migration*, no. June, pp. 249–260, 2012.

[10] P. P. Provenzano, D. R. Inman, K. W. Eliceiri, J. G. Knittel, L. Yan, C. T. Rueden, J. G. White, and P. J. Keely, "Collagen density promotes mammary tumor initiation and progression.," *BMC medicine*, vol. 6, p. 11, Jan. 2008.

[11] M. D. Amatangelo, D. E. Bassi, A. J. P. Klein-Szanto, and E. Cukierman, "Stroma-derived three-dimensional matrices are necessary and sufficient to promote desmoplastic differentiation of normal fibroblasts.," *The American journal of pathology*, vol. 167, no. 2, pp. 475–88, Aug. 2005.

[12] M. L. Taddei, E. Giannoni, G. Comito, and P. Chiarugi, “Microenvironment and tumor cell plasticity: an easy way out.,” *Cancer letters*, vol. 341, no. 1, pp. 80–96, Nov. 2013.

[13] M. W. Conklin, J. C. Eickhoff, K. M. Riching, C. a Pehlke, K. W. Eliceiri, P. P. Provenzano, A. Friedl, and P. J. Keely, “Aligned collagen is a prognostic signature for survival in human breast carcinoma.,” *The American journal of pathology*, vol. 178, no. 3, pp. 1221–32, Mar. 2011.

[14] P. Friedl and K. Wolf, “Plasticity of cell migration: a multiscale tuning model.,” *The Journal of cell biology*, vol. 188, no. 1, pp. 11–9, Jan. 2010.

[15] J. Condeelis and J. E. Segall, “Intravital imaging of cell movement in tumours.,” *Nature reviews. Cancer*, vol. 3, no. 12, pp. 921–30, Dec. 2003.

[16] K. Wolf and P. Friedl, “Extracellular matrix determinants of proteolytic and non-proteolytic cell migration.,” *Trends in cell biology*, vol. 21, no. 12, pp. 736–44, Dec. 2011.

[17] T. D. Palmer, W. J. Ashby, J. D. Lewis, and A. Zijlstra, “Targeting tumor cell motility to prevent metastasis.,” *Advanced drug delivery reviews*, vol. 63, no. 8, pp. 568–81, Jul. 2011.

[18] J. Albuschies and V. Vogel, “The role of filopodia in the recognition of nanotopographies,” *Scientific Reports*, vol. 3, Apr. 2013.

[19] J. C. Adams, “Cell-Matrix Contact Structures,” *Cellular and Molecular Life Sciences*, vol. 58, pp. 371–392, 2001.

[20] P. Friedl and K. Wolf, “Tumour-cell invasion and migration: diversity and escape mechanisms.,” *Nature reviews. Cancer*, vol. 3, no. 5, pp. 362–74, May 2003.

[21] J. Faix, D. Breitsprecher, T. E. B. Stradal, and K. Rottner, “Filopodia: Complex models for simple rods.,” *The international journal of biochemistry & cell biology*, vol. 41, no. 8–9, pp. 1656–64, 2009.

[22] D. a Murphy and S. a Courtneidge, “The ‘ins’ and ‘outs’ of podosomes and invadopodia: characteristics, formation and function.,” *Nature reviews. Molecular cell biology*, vol. 12, no. 7, pp. 413–26, Jul. 2011.

[23] C. Le Clainche and M.-F. Carlier, “Regulation of actin assembly associated with protrusion and adhesion in cell migration,” *PHYSIOLOGICAL REVIEWS*, vol. 88, no. 2, pp. 489–513, Apr. 2008.

[24] R. L. Klemke, “Trespassing cancer cells: ‘fingerprinting’ invasive protrusions reveals metastatic culprits.,” *Current opinion in cell biology*, vol. 24, no. 5, pp. 662–9, Oct. 2012.

[25] J. S. Condeelis, J. B. Wyckoff, M. Bailly, R. Pestell, D. Lawrence, J. Backer, and J. E. Segall, "Lamellipodia in invasion.," *Seminars in cancer biology*, vol. 11, no. 2, pp. 119–28, May 2001.

[26] M. Schoumacher, R. D. Goldman, D. Louvard, and D. M. Vignjevic, "Actin, microtubules, and vimentin intermediate filaments cooperate for elongation of invadopodia.," *The Journal of cell biology*, vol. 189, no. 3, pp. 541–56, May 2010.

[27] J. Oyanagi, T. Ogawa, H. Sato, S. Higashi, and K. Miyazaki, "Epithelial-mesenchymal transition stimulates human cancer cells to extend microtubule-based invasive protrusions and suppresses cell growth in collagen gel.," *PloS one*, vol. 7, no. 12, p. e53209, Jan. 2012.

[28] A. Giri, S. Bajpai, N. Trenton, H. Jayatilaka, G. D. Longmore, and D. Wirtz, "The Arp2/3 complex mediates multigeneration dendritic protrusions for efficient 3-dimensional cancer cell migration.," *FASEB journal : official publication of the Federation of American Societies for Experimental Biology*, pp. 1–11, Jun. 2013.

[29] S. Wong, W.-H. Guo, and Y.-L. Wang, "Fibroblasts probe substrate rigidity with filopodia extensions before occupying an area.," *Proceedings of the National Academy of Sciences of the United States of America*, vol. 111, no. 48, pp. 1–6, Nov. 2014.

[30] K. M. Riching, B. L. Cox, M. R. Salick, C. Pehlke, A. S. Riching, S. M. Ponik, B. R. Bass, W. C. Crone, Y. Jiang, A. M. Weaver, K. W. Eliceiri, and P. J. Keely, "3D Collagen Alignment Limits Protrusions to Enhance Breast Cancer Cell Persistence.," *Biophysical journal*, vol. 107, no. 11, pp. 2546–58, Dec. 2014.

[31] D. T. Burnette, S. Manley, P. Sengupta, R. Sougrat, M. W. Davidson, B. Kachar, and J. Lippincott-Schwartz, "A role for actin arcs in the leading-edge advance of migrating cells.," *Nature cell biology*, vol. 13, no. 4, pp. 371–81, Apr. 2011.

[32] N. S. Gov and A. Gopinathan, "Dynamics of membranes driven by actin polymerization.," *Biophysical journal*, vol. 90, no. 2, pp. 454–69, Jan. 2006.

[33] a Ponti, M. Machacek, S. L. Gupton, C. M. Waterman-Storer, and G. Danuser, "Two distinct actin networks drive the protrusion of migrating cells.," *Science (New York, N.Y.)*, vol. 305, no. 5691, pp. 1782–6, Sep. 2004.

[34] D. Zicha, I. M. Dobbie, M. R. Holt, J. Monypenny, D. Y. H. Soong, C. Gray, and G. a Dunn, "Rapid actin transport during cell protrusion.," *Science (New York, N.Y.)*, vol. 300, no. 5616, pp. 142–5, Apr. 2003.

[35] A. S. Meyer, S. K. Hughes-Alford, J. E. Kay, A. Castillo, A. Wells, F. B. Gertler, and D. a Lauffenburger, "2D protrusion but not motility predicts growth factor-induced cancer cell migration in 3D collagen.," *The Journal of cell biology*, vol. 197, no. 6, pp. 721–9, Jun. 2012.

[36] P. G. Gritsenko, O. Ilina, and P. Friedl, “Interstitial guidance of cancer invasion.,” *The Journal of pathology*, vol. 226, no. 2, pp. 185–99, Jan. 2012.

[37] P. Lu, V. M. Weaver, and Z. Werb, “The extracellular matrix: a dynamic niche in cancer progression.,” *The Journal of cell biology*, vol. 196, no. 4, pp. 395–406, Mar. 2012.

[38] J. Brábek, C. T. Mierke, D. Rösel, P. Veselý, and B. Fabry, “The role of the tissue microenvironment in the regulation of cancer cell motility and invasion.,” *Cell communication and signaling : CCS*, vol. 8, p. 22, Jan. 2010.

[39] A. C. Hielscher, C. Qiu, and S. Gerecht, “Breast cancer cell-derived matrix supports vascular morphogenesis.,” *American journal of physiology. Cell physiology*, vol. 302, no. 8, pp. C1243–56, Apr. 2012.

[40] A. Patsialou, Y. Wang, J. Lin, K. Whitney, S. Goswami, P. a Kenny, and J. S. Condeelis, “Selective gene-expression profiling of migratory tumor cells in vivo predicts clinical outcome in breast cancer patients.,” *Breast cancer research : BCR*, vol. 14, no. 5, p. R139, Oct. 2012.

[41] S. Meehan and A. S. Nain, “Role of Suspended Fiber Structural Stiffness and Curvature on Single-Cell Migration, Nucleus Shape, and Focal-Adhesion-Cluster Length,” *Biophysical Journal*, vol. 107, no. 11, pp. 2604–2611, Dec. 2014.

[42] A. S. Nain, M. Sitti, A. Jacobson, T. Kowalewski, and C. Amon, “Dry Spinning Based Spinneret Based Tunable Engineered Parameters (STEP) Technique for Controlled and Aligned Deposition of Polymeric Nanofibers.,” *Macromolecular rapid communications*, vol. 30, no. 16, pp. 1406–12, Aug. 2009.

[43] A. S. Nain, J. A. Phillippi, M. Sitti, J. Mackrell, P. G. Campbell, and C. Amon, “Control of cell behavior by aligned micro/nanofibrous biomaterial scaffolds fabricated by spinneret-based tunable engineered parameters (STEP) technique.,” *Small (Weinheim an der Bergstrasse, Germany)*, vol. 4, no. 8, pp. 1153–9, Aug. 2008.

[44] J. Wang and A. S. Nain, “Suspended Micro/Nanofiber Hierarchical Biological Scaffolds Fabricated using Non-Electrospinning STEP Technique.,” *Langmuir : the ACS journal of surfaces and colloids*, vol. 30, no. 45, pp. 13641–13649, Oct. 2014.

[45] A. S. Nain and J. Wang, “Polymeric nanofibers: isodiametric design space and methodology for depositing aligned nanofiber arrays in single and multiple layers,” *Polymer Journal*, pp. 1–6, Feb. 2013.

[46] and A. S. N. Kevin Sheets, Ji Wang, Sean Meehan, Puja Sharma, Colin Ng, Mohammad Khan, Brian Koons, Bahareh Behkam, “Cell-Fiber Interactions on Aligned and Suspended Nanofiber Scaffolds Kevin,” *Journal of Biomaterials and Tissue Engineering*, 2013.

[47] P. Sharma, K. Sheets, S. Elankumaran, and A. S. Nain, "The mechanistic influence of aligned nanofibers on cell shape, migration and blebbing dynamics of glioma cells.," *Integrative biology : quantitative biosciences from nano to macro*, vol. 5, no. 8, pp. 1036–44, Aug. 2013.

[48] D. C. Alexander, P. L. Hubbard, M. G. Hall, E. a Moore, M. Ptito, G. J. M. Parker, and T. B. Dyrby, "Orientationally invariant indices of axon diameter and density from diffusion MRI.," *NeuroImage*, vol. 52, no. 4, pp. 1374–89, Oct. 2010.

[49] T. a Ulrich, E. M. de Juan Pardo, and S. Kumar, "The mechanical rigidity of the extracellular matrix regulates the structure, motility, and proliferation of glioma cells.," *Cancer research*, vol. 69, no. 10, pp. 4167–74, May 2009.

[50] F. Lefranc, J. Brotchi, and R. Kiss, "Possible future issues in the treatment of glioblastomas: special emphasis on cell migration and the resistance of migrating glioblastoma cells to apoptosis.," *Journal of clinical oncology : official journal of the American Society of Clinical Oncology*, vol. 23, no. 10, pp. 2411–22, Apr. 2005.

[51] D. Zicha, I. M. Dobbie, M. R. Holt, J. Monypenny, D. Y. H. Soong, C. Gray, and G. a Dunn, "Rapid actin transport during cell protrusion.," *Science (New York, N.Y.)*, vol. 300, no. 5616, pp. 142–5, Apr. 2003.

[52] E. S. Welf, S. Ahmed, H. E. Johnson, A. T. Melvin, and J. M. Haugh, "Migrating fibroblasts reorient directionality by a metastable, PI3K-dependent mechanism.," *The Journal of cell biology*, vol. 197, no. 1, pp. 105–14, Apr. 2012.

[53] A. Nimmerjahn, F. Kirchhoff, and F. Helmchen, "Resting microglial cells are highly dynamic surveillants of brain parenchyma in vivo.," *Science (New York, N.Y.)*, vol. 308, no. 5726, pp. 1314–8, May 2005.

[54] J.-L. Hoon, W.-K. Wong, and C.-G. Koh, "Functions and regulation of circular dorsal ruffles.," *Molecular and cellular biology*, vol. 32, no. 21, pp. 4246–57, Nov. 2012.

[55] B. Borm, R. P. Requardt, V. Herzog, and G. Kirfel, "Membrane ruffles in cell migration: indicators of inefficient lamellipodia adhesion and compartments of actin filament reorganization.," *Experimental cell research*, vol. 302, no. 1, pp. 83–95, Jan. 2005.

[56] C. Mayer, K. Maaser, N. Daryab, K. S. Zänker, E. B. Bröcker, and P. Friedl, "Release of cell fragments by invading melanoma cells.," *European journal of cell biology*, vol. 83, no. 11–12, pp. 709–15, Dec. 2004.

[57] A. B. Verkhovsky, T. M. Svitkina, and G. G. Borisy, "Self-polarization and directional motility of cytoplasm," *Current Biology*, pp. 11–21, 1999.

[58] K. Wolf, I. Mazo, H. Leung, K. Engelke, U. H. von Andrian, E. I. Deryugina, A. Y. Strongin, E.-B. Bröcker, and P. Friedl, "Compensation mechanism in tumor cell

migration: mesenchymal-amoeboid transition after blocking of pericellular proteolysis.," *The Journal of cell biology*, vol. 160, no. 2, pp. 267–77, Jan. 2003.

[59] A. D. Lieber, S. Yehudai-Resheff, E. L. Barnhart, J. a Theriot, and K. Keren, "Membrane tension in rapidly moving cells is determined by cytoskeletal forces.," *Current biology : CB*, vol. 23, no. 15, pp. 1409–17, Aug. 2013.

[60] E. Cocucci, G. Racchetti, and J. Meldolesi, "Shedding microvesicles: artefacts no more.," *Trends in cell biology*, vol. 19, no. 2, pp. 43–51, Feb. 2009.

[61] Z. Li, J. Song, G. Mantini, M.-Y. Lu, H. Fang, C. Falconi, L.-J. Chen, and Z. L. Wang, "Quantifying the traction force of a single cell by aligned silicon nanowire array.," *Nano letters*, vol. 9, no. 10, pp. 3575–80, Oct. 2009.

[62] I. Indra, V. Undyala, C. Kandow, U. Thirumurthi, M. Dembo, and K. a Beningo, "An in vitro correlation of mechanical forces and metastatic capacity.," *Physical biology*, vol. 8, no. 1, p. 015015, Feb. 2011.

APPENDIX A

Analysis of fibronectin coating on fibers

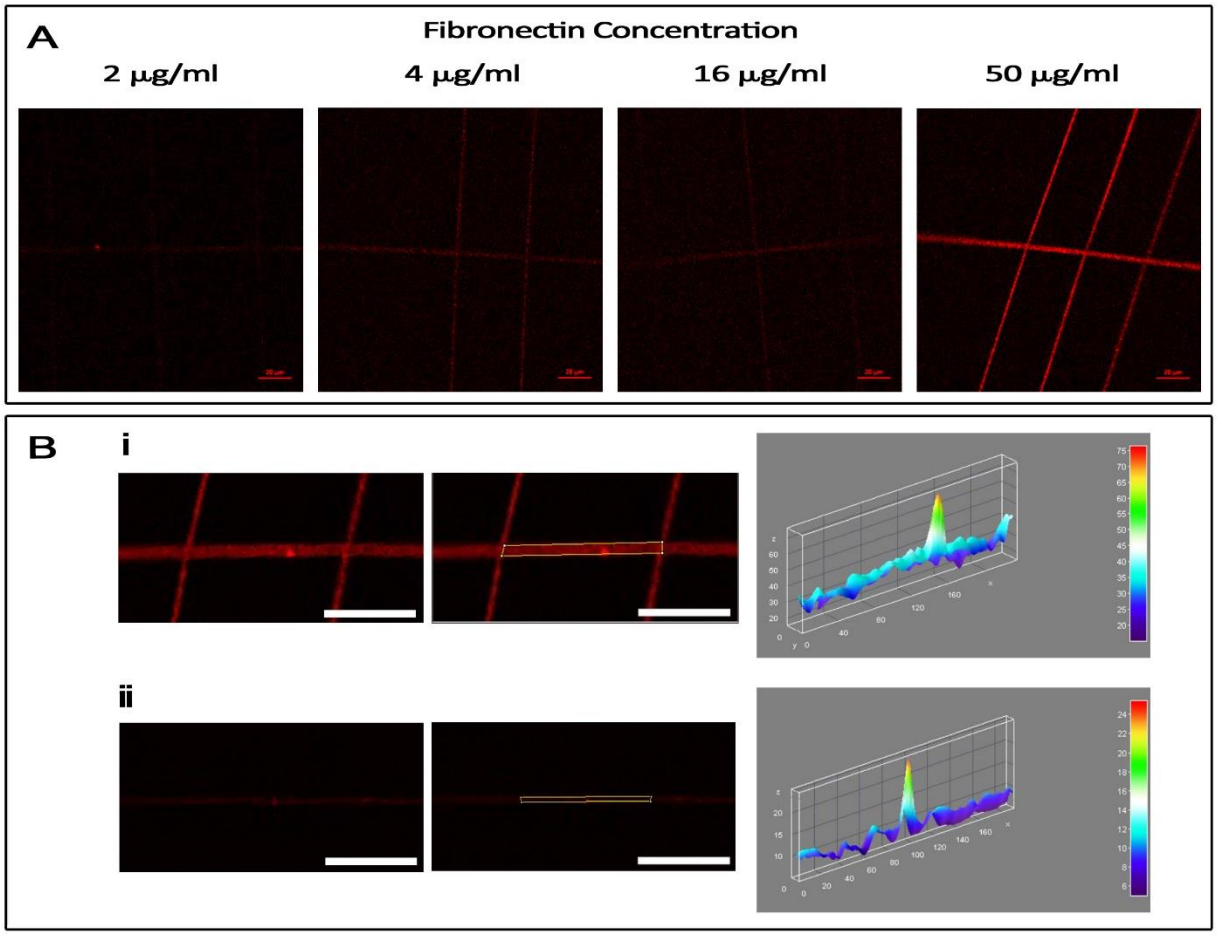

Figure A.1 Fibronectin coating analysis shows higher presence of fibronectin on fibers coated with higher concentrations as well as regions with a higher amount of fibronectin on the same sample. (A) Fiber samples of same diameter coated with 2, 4, 16, and 50 µg/ml concentration of a fluorescent fibronectin solution. Images were taken using confocal microscopy and the fluorescent signal shown increases with concentration except between the 4 and 16 µg/ml concentrations. (B) Intensity of the fluorescent signal was analyzed throughout sections of the fibers that visibly showed regions with higher intensities. The intensity profiles of fibers coated with (i) 50 µg/ml and (ii) 4 µg/ml show that, among the same sample coated with the same concentration, there are regions along the fibers that have more fibronectin present.

APPENDIX B

Derivation of the fiber bending differential equation

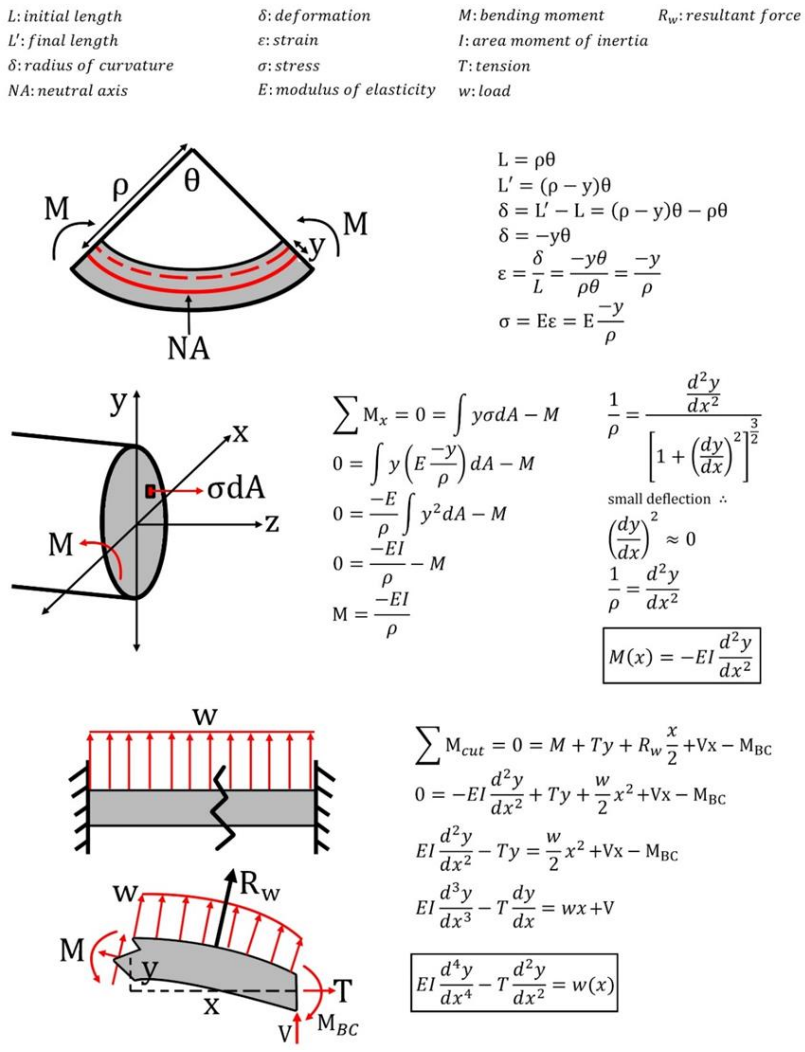

Figure B.1 Derivation of the differential equation that describes the fiber deflection profile shows the underlying theory, assumptions, and mechanics of the system. The differential equation shown outlined at the bottom is the differential equation used in the force mathematical model.

APPENDIX C

Mathematica code of mathematical force model

The following is the Wolfram Mathematica code used for the ramp distributed load condition:

```
Manipulate[
 (*Model Constants*)
 Elast = 3 (* nN/um^2*); Dia = 550 (*um*);
 MoI = \[Pi]/64*(Dia)^4    (*um^4*);
 TenStress = 4.1*10^-3 (*nN/um^2 --> 4.1 MPa*);
 area = \[Pi]/4*(Dia)^2   (*nm^2*);
 Ten = TenStress*area  (*nN*); L = Length*10^3(*nm*);
 a = Apos*10^3;
 b = Bpos*10^3;
 z = b - a;
 yL = 0; yH = 5; xL = 0; xH = L; fL = 0; fH = LeftLoad*1.5;
 RightLoad = 0;
 LeftLoad = LL*0.001; (*nN/nm --\[Rule] 1 nN/um = 1000 nm/um*)
 FanLoad = LeftLoad*(UnitStep[x - a] - UnitStep[x - (a + z)]);
 LL = LeftLoad*1000;
 slope = (RightLoad - LeftLoad)/((a + z) - a);
 RampLoad = (slope*(x - a) + LeftLoad)*(UnitStep[x - a] -
    UnitStep[x - (a + z)]);
 Fresultant = 1/2*(z*0.001)*(LeftLoad*1000);
 Fanresultant = (z*0.001)*(FanLoad*1000);
 xFanR = a + 1/2*z;
 xFR = a + 1/3*z;
 Off[NDSolve::precw];
 Off[NDSolve::berr];
 Off[NDSolve::bvluc];
 eqn = Elast*MoI*y""[x] - Ten*y"[x] == RampLoad;
 bcs = {y[0] == 0, y[L] == 0, y'[0] == 0, y'[L] == 0};
 solx4 = NDSolve[{eqn, bcs}, y, x,
   Method -> {"Shooting",
     "StartingInitialConditions" -> {y[x4*10^3] == 0,
       y'[x4*10^3] == 0}}, InterpolationOrder -> All,
   WorkingPrecision -> 50, PrecisionGoal -> 10, AccuracyGoal -> 10];
 solx2 = NDSolve[{eqn, bcs}, y, x,
   Method -> {"Shooting",
     "StartingInitialConditions" -> {y[x2*10^3] == 0,
       y'[x2*10^3] == 0}}, InterpolationOrder -> All,
   WorkingPrecision -> 50, PrecisionGoal -> 10, AccuracyGoal -> 10];
 MeasuredPoints =
  Import[NotebookDirectory[] <> "expinput.xlsx", {"Sheets", 2}];
 mp = ListPlot[MeasuredPoints, PlotRange -> {{xL, xH}, {yL, yH}},
```

```
  ImageSize -> 400; AspectRatio -> 0.5, PlotStyle -> Darker[Green],
  PlotMarkers -> {Automatic, Large}];
points = MeasuredPoints[[All, 1]]; (*vector of X positions in nm *)
x1 = points[[1]]*0.001; (*All five in um*)
x2 = points[[2]]*0.001;
x3 = points[[3]]*0.001;
x4 = points[[4]]*0.001;
x5 = points[[5]]*0.001;
thick = 0.01;
InputFunct =
 Plot[RampLoad, {x, 0, L}, PlotRange -> {{xL, xH}, {fL, fH}},
  PlotStyle -> {{Red, Thickness[thick]}},
  AxesStyle -> {Directive[Black, Thick, 16],
    Directive[Black, Thick, 16]}, ImageSize -> 400, Filling -> Axis,
  AspectRatio -> 0.3];
OutputFunctx4 =
 Plot[{(y[x] /. solx4)*0.001}, {x, a, L},
  PlotRange -> {{xL, xH}, {yL, yH}},
  PlotStyle -> {{Blue, Thickness[thick], Opacity[0.5]}},
  AxesStyle -> {Directive[Black, Thick, 16],
    Directive[Black, Thick, 16]}, ImageSize -> 400,
  AspectRatio -> 0.5];
OutputFunctx2 =
 Plot[{(y[x] /. solx2)*0.001}, {x, 0, a},
  PlotRange -> {{xL, xH}, {yL, yH}},
  PlotStyle -> {{Blue, Thickness[thick], Opacity[0.5]}},
  AxesStyle -> {Directive[Black, Thick, 16],
    Directive[Black, Thick, 16]}, ImageSize -> 400,
  AspectRatio -> 0.5];
BothOutput =
 Show[{{mp}, {OutputFunctx4}, {OutputFunctx2}}, ImageSize -> 400,
  AxesStyle -> {Directive[Black, Thick, 16],
    Directive[Black, Thick, 16]}];
yFR = (y[xFR] /. solx4)*0.001;
stiff = Fresultant/yFR;
Grid[{{InputFunct}, {BothOutput}}],
"Force Function Inputs",
Delimiter,
{{LL, 1.5, "Left Load [nN/um]"}, 0, 40},
TextCell["Resultant Force [nN]:", "Text"],
Dynamic[Framed[Fresultant]],
TextCell["Stiffness [nN/um]:", "Text"],
Dynamic[Framed[stiff]],
Delimiter,
{{Length, x5, "Fiber Length [um]"}, 0, 500},
Delimiter,
```

```
{{Apos, x2, "A - Near Position"}, 0, 1000},
{{Bpos, x4, "B - Far Position"}, 0, 1000},
Delimiter,
{{r, x4, "IVP Location"}, 0, 1000},
ContinuousAction -> False, ControlPlacement -> Left]
```

APPENDIX D

MATLAB code of mathematical force model

The following is the MathWorks MATLAB code used for the distributed load condition:

```
function DistLoad_Final_auto3
clear all
clc
elast=3*10^(-9);
dia=600;
moi=(3.14/64)*dia^4;
tenstress=4.1*10^(-12); % tensile stress = 4.1 MPa
area=(3.14/4)*dia^2;
ten=tenstress*area;
%Measured Coordinates
%Points [um]
%INSERT COORDINATES HERE ----- in [um]
%x1=     0     ;     y1=     0     ;
%x2=  53.9  ;     y2= 10.95;
%x3=  64.47     ;   y3= 12.28;
%x4=   91.16  ;     y4= 10.3 ;
%x5=    185.09    ;     y5=     0     ;
input=xlsread('input.xls',1,'A1:DP5');
exp=input*10^(-3);
count=0;
for n=1:2:119
wmag=0;
a=exp(2,n);
b=exp(4,n);
L=exp(5,n);
xlow=0; xhigh=L;
set=0;
   while set==0;
   solinit = bvpinit(linspace(xlow,xhigh,10),[0 0 0 0]);
   sol=bvp4c(@bvp4ode,@bvp4bc,solinit);
   xint=linspace(xlow,xhigh,1000);   % # number is how dense the mesh is
   Sxint=deval(sol,xint);
   modelmin=abs(min(Sxint(1,:)));
   expmin=abs(exp(3,n+1));
   error= 100*(modelmin./expmin);
   fprintf('wmag--%6.5f--error--%3.2f\n',wmag,error);
      if error<50;
         wmag=wmag+1000;
      elseif error>50 && error<85
         wmag=wmag+500;
```

```
        elseif error>85 && error<95
            wmag=wmag+100;
        elseif error>95 && error<98;
            wmag=wmag+50;
        else
            solvector(n)=wmag*10^(-6);
            set=1;
        end
    end
count=count+1;
countset(count)=count;
solutionset(count)=wmag*1000; %nN/um
SolutionList=transpose(solvector);
fprintf('#:%3.0f',count)
fprintf('---HighRampLoad:%6.5f',wmag*10^(-6))
fprintf('--LowRampLoad:%1.0f\n',0)
%OUTPUTS----------------------
%Numerical Values
%Input_Load_Magnitude=wmag;
%Resultant_Force_Magnitude=wmag*(b-a)
%Max_Deflection_Model=min(Sxint(1,:))
%Max_Deflection_Exp=exp(3,2)
%Percent_Error_at_MaxD= (abs(Max_Deflection_Model-
Max_Deflection_Exp)/abs(Max_Deflection_Exp))*100
%x_exp=exp(:,1);
%y_exp=exp(:,2);
%p=polyfit(x_exp,y_exp,3);
%pv=polyval(p,x_exp);
%Plots
%plot(xint,Sxint(1,:));
%hold on;
%plot(x_exp,y_exp,'o',x_exp,pv,'-');
%hold off;
end
plot(countset,solutionset);
%-------------------------
function [dydx]=bvp4ode(x,y)
%elast=3*10^9;
%dia=500*10^(-9);
%moi=(3.14/64)*dia^4;
%tenstress=4.1*10^6; % tensile stress = 4.1 MPa
%area=(3.14/4)*dia^2;
%ten=tenstress*area;
%INSERT COORDINATES HERE
%load
slope= (-1*wmag)/(a-b);
```

```
w_ramp= (slope*(x-a)+(-1*wmag))*(heaviside(x-a)-heaviside(x-b));
w_uniform=(-1*wmag)*(heaviside(x-a)-heaviside(x-b));
w_point_mid=(-1*wmag)*(heaviside(x-0.5*(a+b))-heaviside(x-1.1*(0.5*(a+b))));
w_point_a=(-1*wmag)*(heaviside(x-a)-heaviside(x-1.1*a));
w_point_b=(-1*wmag)*(heaviside(x-b)-heaviside(x-1.1*b));
w_point_bothends=(-1*wmag)*(heaviside(x-a)-heaviside(x-1.1*a))+(-1*wmag)*(heaviside(x-
b)-heaviside(x-1.1*b));
sslope=(-1*wmag)/(a-((a+b)/2));
w_ramp_two= (sslope*(x-a)+(-1*wmag))*(heaviside(x-a)-heaviside(x-((a+b)/2)))+((-
1*sslope)*(x-b)+(-1*wmag))*(heaviside(x-((a+b)/2))-heaviside(x-b));
dydx=[
    y(2)
    y(3)
    y(4)
   (1/(elast*moi))*(w_ramp+ten*y(3))
    ];end
%------------------------
function res=bvp4bc(ya,yb)
res=[
    ya(1)
    ya(2)
    yb(1)
    yb(2)
    ];end
end
```